Check for updates

AGU ADVANCING EARTH AND SPACE SCIENCE

Water Resources Research

RESEARCH ARTICLE
10.1029/2021WR030606

# Flood Extent Mapping During Hurricane Florence With Repeat-Pass L-Band UAVSAR Images

**Chao Wang[1], Tamlin M. Pavelsky[1], Fangfang Yao[2], Xiao Yang[1], Shuai Zhang[3], Bruce Chapman[4], Conghe Song[5], Antonia Sebastian[1], Brian Frizzelle[6], Elizabeth Frankenberg[7], and Nicholas Clinton[8]**

[1]Department of Earth, Marine and Environmental Sciences, University of North Carolina, Chapel Hill, NC, USA, [2]CIRES University of Colorado Boulder, Boulder, CO, USA, [3]College of Marine Science, University of South Florida, St. Petersburg, FL, USA, [4]Jet Propulsion Laboratory, California Institute of Technology, Pasadena, CA, USA, [5]Department of Geography, University of North Carolina, Chapel Hill, NC, USA, [6]Carolina Population Center, University of North Carolina, Chapel Hill, NC, USA, [7]Department of Sociology and Carolina Population Center, University of North Carolina, Chapel Hill, NC, USA, [8]Google, Inc., Mountain View, CA, USA

**Abstract** Extreme precipitation events are intensifying due to a warming climate, which, in some cases, is leading to increases in flooding. Detection of flood extent is essential for flood disaster response, management, and prevention. However, it is challenging to delineate inundated areas through most publicly available optical and short-wavelength radar data, as neither can "see" through dense forest canopies. In 2018, Hurricane Florence produced heavy rainfall and subsequent record-setting riverine flooding in North Carolina, USA. NASA/JPL collected daily high-resolution full-polarized L-band Uninhabited Aerial Vehicle Synthetic Aperture Radar (UAVSAR) data between September 18th and 23rd. Here, we use UAVSAR data to construct a flood inundation detection framework through a combination of polarimetric decomposition methods and a Random Forest classifier. Validation of the established models with compiled ground references shows that the incorporation of linear polarizations with polarimetric decomposition and terrain variables significantly enhances the accuracy of inundation classification, and the Kappa statistic increases to 91.4% from 64.3% with linear polarizations alone. We show that floods receded faster near the upper reaches of the Neuse, Cape Fear, and Lumbee Rivers. Meanwhile, along the flat terrain close to the lower reaches of the Cape Fear River, the flood wave traveled downstream during the observation period, resulting in the flood extent expanding 16.1% during the observation period. In addition to revealing flood inundation changes spatially, flood maps such as those produced here have great potential for assessing flood damages, supporting disaster relief, and assisting hydrodynamic modeling to achieve flood-resilience goals.

**Key Points:**

- Quad-polarized L-band UAVSAR and scattering mechanisms polarimetric decomposition leads to the high accuracy of flood extent mapping
- The normalization of the incidence angle effectively corrects the backscatter brightness that gradually decreases along the range direction
- Dense UAVSAR time series reveal detailed flood extent variability, consistent with water height recorded at USGS gages

**Supporting Information:**

Supporting Information may be found in the online version of this article.

**Correspondence to:**

C. Wang,
waynechao128@gmail.com;
chao.wang@unc.edu

**Citation:**

Wang, C., Pavelsky, T. M., Yao, F., Yang, X., Zhang, S., Chapman, B., et al. (2022). Flood extent mapping during Hurricane Florence with repeat-pass L-band UAVSAR images. *Water Resources Research*, *58*, e2021WR030606. https://doi.org/10.1029/2021WR030606

Received 22 JUN 2021
Accepted 6 FEB 2022
corrected 20 MAY 2022

This article was corrected on 20 MAY 2022. See the end of the full text for details.

© 2022. American Geophysical Union. All Rights Reserved.

## 1. Introduction

Floods are the most frequent, disastrous, and widespread natural hazards, accounting for more than 70% of hazard events occurring globally between 1994 and 2013 (UNISDR, 2015). Between 1851 and 2017, more than three hundred hurricanes hit the U.S. East and Gulf coasts, causing massive damage, and upending the lives of millions (Song et al., 2018). Recent studies project that ongoing global climate change favors increased intensity of extreme precipitation events (Bender et al., 2010; Prein et al., 2017) and a resulting increase risk of flood exposure (Alfieri et al., 2017; Dottori et al., 2018). Flood risk is especially increasing in low-lying coastal regions that are densely populated with some of the most valuable property worldwide (Kron, 2013; Qiang, 2019; Rueda et al., 2017). By 2050, worldwide annual losses due to flooding are projected to reach US $1 trillion for coastal cities (Hallegatte et al., 2013).

To achieve the goals of disaster risk reduction and sustainable development, governments and non-governmental organizations (NGOs) require access to near-real-time high-quality flood maps (Martinis et al., 2009; Schumann, 2014). For instance, flood inventory maps are useful in supporting flood damage assessment (Chaabani et al., 2018), calibration and validation of flood inundation (i.e., hydraulic) models (Giustarini et al., 2015; Shin et al., 2020), climate change adaptation policies (e.g., flood risk mitigation planning; Razavi et al., 2020), and the development of public disaster relief solutions (e.g., Flood Insurance Rate Maps; Cian et al., 2018). The reliability of these maps directly affects the subsequent analysis and the effectiveness of relief policies (Hoch et al., 2019).

Airborne and spaceborne Earth observation platforms have revolutionized the monitoring of inundation dynamics immediately following flood events (Dewan et al., 2006; Nateghi et al., 2016; Pradhan et al., 2016). Rapid progress has been made in flood detection algorithms that use optical images to assess flood events (Ban et al., 2017). Many early studies were based on relatively low spatial resolution imagery (≥250 m), such as images from the Advanced Very High-Resolution Radiometer (AVHRR) and Moderate Resolution Imaging Spectrometer (MODIS; Ali et al., 1989; Brakenridge & Anderson, 2006; Sanyal & Lu, 2004). These studies usually explore the advantage of daily satellite observations to partially compensate for limitations associated with cloud cover (Heimhuber et al., 2018). But poor spatial resolution of these satellite observations makes it difficult to accurately monitor changes in inundation extent of many small, narrow rivers and some larger ones with irregular shapes. It is common today to use optical imagery with a spatial resolution of 30 m or finer (e.g., Landsat and Sentinel 2 missions) for flood monitoring (Caballero et al., 2019). However, long revisit time of fine spatial resolution satellite observations and persistent cloud cover during extreme weather events continue to limit the use of optical imagery for rapid response flood mapping (Ban et al., 2017; Bioresita et al., 2018).

In contrast to optical imagery, synthetic aperture radar (SAR) systems characterize Earth's surface independent of weather conditions (Smith, 1997). Due to high radar reflectivity differences between land and water associated with water's high dielectric constant, SAR has become particularly useful for mapping flood inundation (Brisco et al., 2009; Hess et al., 2003; Santoro & Wegmüller, 2014). This is especially true in situations with persistent cloud cover, common during major flood events, when SAR provides a unique capacity for disaster monitoring (Ohki & Shimada, 2018; Twele et al., 2016). The relevant scientific literature has grown rapidly over the last decade, coinciding more or less with recent launches of Earth-orbiting satellites carrying SAR instruments (e.g., PALSAR-2, Sentinel-1, Radarsat-2, TerraSAR-X, and Cosmo-SkyMed; Benoudjit & Guida, 2019; Cao et al., 2019; Clement et al., 2018; Huang et al., 2018). These SAR platforms have provided unprecedented L-, C-, and X-band observations of the Earth's land surface, all of which have been successfully used to monitor flood dynamics (Bioresita et al., 2018; Chapman et al., 2015; Shen, Wang, et al., 2019). It is worth noting that longer wavelength (e.g., L-band) SAR signals better penetrate vegetation canopy and undergo multiple scattering between the canopy, trunks, and forest floor or subcanopy inundation. Therefore, they are generally seen as superior to shorter wavelength SAR signals (e.g., X- or C-band) for flood detection (Hess et al., 1995; Jung et al., 2010; Zhang et al., 2016). In addition, fully polarimetric SAR (i.e., PolSAR) data allows the reconstruction of the complete scattering mechanisms from backscattered signals based on polarimetric decomposition methods, thus achieving an accurate detection of subcanopy inundation (White et al., 2014). However, most spaceborne SAR sensors have been operated to acquire data in single- or dual-polarization mode in nearly all observation configurations. And, due to long revisit times, sparseness of spaceborne SAR observations limits timely capture of flood dynamics (Clement et al., 2018). The dense time series quad-polarized L-band SAR imagery does not suffer from these limitations for flood extent mapping.

The Carolinas have suffered from devastating hurricanes frequently over recent years. In 2018, Hurricane Florence hovered over North Carolina for 6 days, delivering 635–889 mm of precipitation that led to catastrophic riverine flooding. Forty-four of North Carolina's 100 counties, home to an estimated 3.9 million people, were declared federal disaster zones (Cooper, 2018). The National Aeronautics and Space Administration (NASA) Uninhabited Aerial Vehicle Synthetic Aperture Radar (UAVSAR) platform, tasked by the Federal Emergency Management Agency (FEMA), collected substantial amounts of high-resolution quad-polarization airborne L-Band SAR imagery along the main rivers and their tributaries in the aftermath of Hurricane Florence (September 17–23; Lou et al., 2019). Because of the long, narrow shapes and low slopes of the watersheds in eastern North Carolina, the collected UAVSAR imagery coincided with extensive river flooding that occurred in the days after rainfall ceased. For example, flooding on the Lumbee River at Lumberton peaked on September 18th, several days after Florence made landfall, and did not drop below flood stage until October 6th. Therefore, the collected dense time series UAVSAR images provide a unique and valuable opportunity to construct a flood inundation detection framework to repeatedly map rapid changes in flood inundation extents, rather than sparse observations of flood inundation based on spaceborne instruments.

Using this repeat-pass daily UAVSAR data collected in the aftermath of Hurricane Florence, we develop detailed models to capture both open water and subcanopy inundation signals, with advantages in spatial resolution, temporal resolution, and accuracy compared to spaceborne optical or SAR data. To our knowledge, this is the first study to delineate daily inundation extents using multi-temporal quad-polarized L-band UAVSAR images during

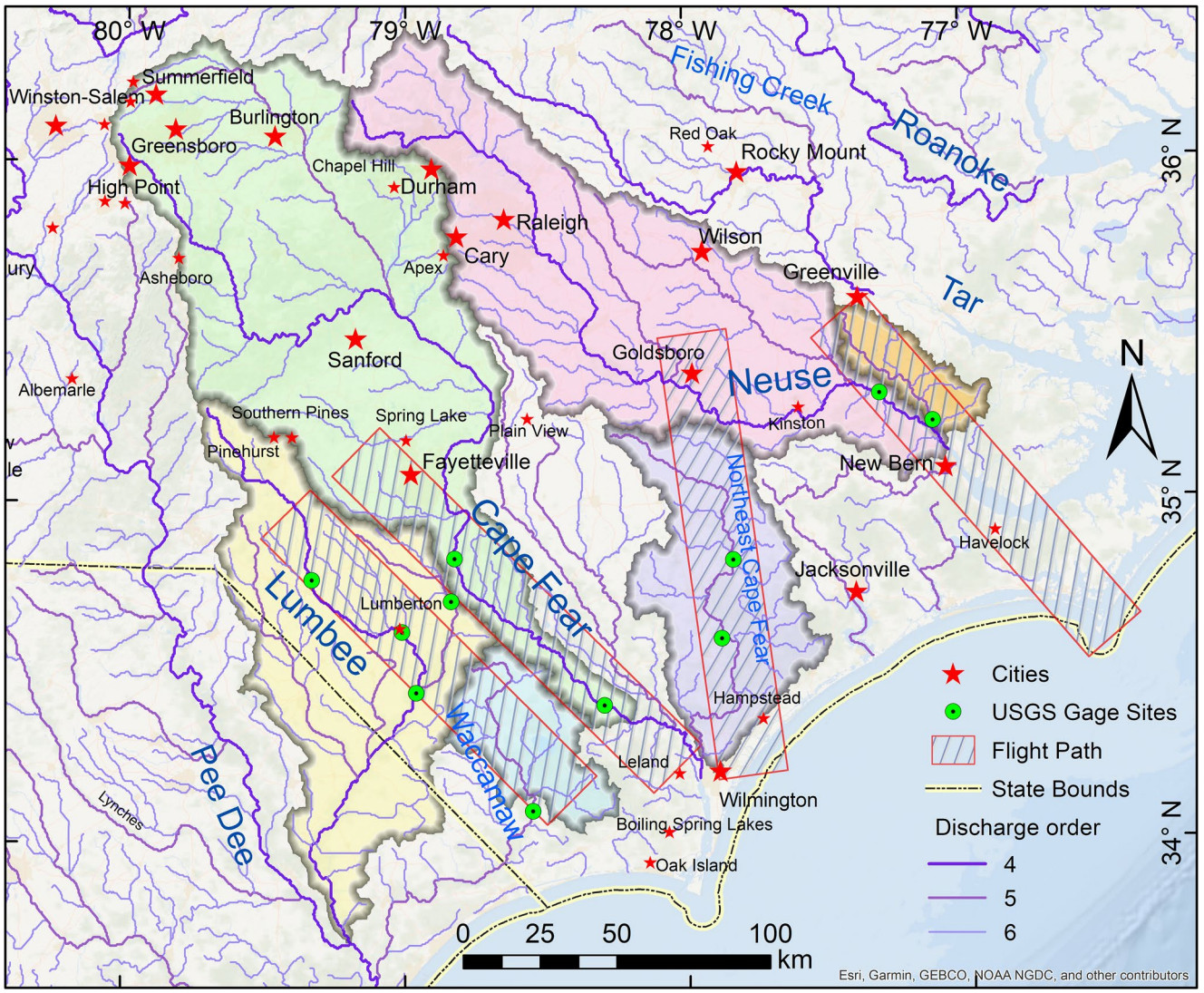


**Figure 1.** Map of four UAVSAR flight lines acquired along the Lower Neuse, Lower Cape Fear, and Lumbee Rivers of North Carolina during the record-breaking floods of September 2018 (Discharge order refers to the Backbone discharge order following the definition from Grill et al. (2019), and 4 refers to 100–1,000 $m^3/s$; 5 refers to 10–100 $m^3/s$ and 6 refers to 1–10 $m^3/s$). USGS gage stations are shown only within the experimental flight lines.

a flood. The specific objectives are to: (i) map inundation extents spatially along floodplains of several big rivers of eastern North Carolina, and (ii) analyze the rapidly changing flood inundation during these observation dates. This work can be extended to future near-real-time flood events response and disaster relief with the UAVSAR system, and can also help extend it to other areas when spaceborne quasi-polarized SAR systems become available on upcoming satellite missions.

## 2. Study Area

The study area is situated in eastern North Carolina's lower coastal plain (Figure 1). Several rivers flow east and southeast across the coastal plain and into the Atlantic Ocean. The local landscape is characterized by a gently sloping terrain with the land cover dominated by cropland, forests, and coastal swampy wetlands. It belongs to a humid subtropical climate (Köppen Climate Classification; Rubel & Kottek, 2010). Specifically, the summer is hot and extremely humid, and the winter is cool with occasional short bouts of cold weather. Rains occur throughout the year but the potential for extreme rainfall events varies seasonally. During the Atlantic hurricane season (June 1 to November 30), extreme rainfall events can occur due to tropical cyclones and their remnants,

especially during the peak period from mid-August through mid-October, which can cause serious flood disasters (Sayemuzzaman & Jha, 2014).

## 3. Methodology

### 3.1. Datasets

#### 3.1.1. UAVSAR Fully Polarimetric Data

UAVSAR's (http://uavsar.jpl.nasa.gov/) fully polarimetric airborne L-band SAR system, flying onboard NASA Armstong's Gulfstream-III, imaged the Hurricane Florence impact area in North Carolina in response to the expected historic flooding; the instrument itself was operated by personnel from NASA's Jet Propulsion Laboratory, who later processed the raw signal data into SAR imagery (Hensley et al., 2008). The L-band UAVSAR is a highly sensitive left-looking SAR with the ability to repeat flight tracks to within 10 m via a precision autopilot control system (Rosen et al., 2006). The radar imaging instrument collects data at an incidence angle range of 22°–67° spanning a 22 km swath in the cross-track direction, and up to 300 km in the along-track direction. The UAVSAR products used in this study are the multi-looked ground range projected (GRD, equiangular) imagery. The pixel spacing is 0.2 arcsec, corresponding to about 6 m by 5 m at the latitude of 35° along the latitude and longitude directions, respectively.

In the week following Hurricane Florence (September 17–23, 2018), NASA collected UAVSAR images of eight flight lines covering several major rivers and their tributaries in eastern North Carolina, with each flight-line imaged two to five times during that time period (Lou et al., 2019). In this study, we focused on four flight lines (i.e., 13510, 31509, 32023, and 35303; Figure 1) with four or more observations between September 18th and September 23rd, corresponding to the area covering the Neuse, Cape Fear, and Lumbee Rivers as well as their tributaries. This is because it allows us to later use these high-frequency daily observations to illustrate rapid temporal variations of inundation extent in hurricane-induced riverine floods. The areas covered are indicated by the hatched polygons in Figure 1 and in Table S1 in Supporting Information S1.

#### 3.1.2. Ground References

Following a flood event, flood extent maps produced by disaster survey experts through visual interpretation and manual digitalization of high-resolution aerial photographs are often considered to be the most reliable reference data (Ohki & Shimada, 2018). These flood extent maps are usually used to validate the accuracy of automated remotely sensed flood detection (Sanyal & Lu, 2004). However, the production of this data is both costly and inefficient, consequently, its availability is limited.

In this study, to collect ground references, we applied a holistic strategy (see the Methods of Supporting Information for step-by-step details) to manually digitized polygons representing different classes. Specifically, first, to avoid bias and ensure generalizability of ground reference collection, we randomly generated 2000 points that overlapped with the UAVSAR flight track covering the Neuse River basin. Then, we collected multisource flood-related dataset such as high-water marks (HWMs, as a reference for inundated and non-inundated locations) collected from the field by the U.S. Geological Survey (USGS) and North Carolina Division of Emergency Management (NCDEM; https://stn.wim.usgs.gov/STNDataPortal/), high-resolution aerial photography (acquired on September 19th–20th, 2018) collected by the National Oceanic and Atmospheric Administration (NOAA; https://storms.ngs.noaa.gov/storms/florence/index.html) during the period of flooding, high-resolution satellite imagery (acquired on September 21st, 2018) from Google Earth Pro, and UAVSAR-derived false color Pauli polarimetric decomposition image (Figure S1b in Supporting Information S1). Note that HWMs are traces of a given point indicating a certain height under flood water. Because they are collected posterior to the event, HWMs do not have date information specific to the time of peak flooding. However, they can still be used as evidence of inundated/non-inundated conditions near the site (Schaffer-Smith et al., 2020), thus aiding visual interpretation of high-resolution aerial/satellite imagery from NOAA and Google Earth (with specific collection date information) to identify flood hotspots and manually digitized ground reference polygons. Finally, by overlaying the randomly generated points with these flood-related datasets (such as HWM and high-resolution aerial/satellite imagery), we manually digitized polygons near each point and visually interpreted and labeled them in 9 different classes (Figure S1a and Table S3 in Supporting Information S1), including open surface water, open herbaceous vegetation on flood waters, sparse trees in flood waters, inundation beneath forest, wet grassland

(or unharvested cropland), dry grassland (or fallow cropland dominated by bare soil), grass-dominated mosaic landscape, tree-dominated mosaic landscape, and upland forest. Note that we can determine where inundated/non-inundated classes are from high-resolution aerial/satellite imagery, but cannot ensure the homogeneity of inundated classes within subsequently digitized polygons, especially for dense canopy regions. UAVSAR-derived false color Pauli polarimetric decomposition image (Figure S1b in Supporting Information S1) can be interpreted as additional auxiliary information. After preparing the digitized reference polygons, we randomly generated reference sample points based on the area of the polygons. Specifically, we randomly generated seven points per 1,000 $m^2$ for each polygon, except for polygons smaller than 1,000 $m^2$, where seven random points are taken. This resulted in total 18,010 ground reference points.

#### 3.1.3. Terrain Variables and Other Auxiliary Datasets

The digital elevation model (DEM) data used in this study was downloaded from North Carolina State University Libraries (Newcomb & Terziotti, 2013). It was derived from LIDAR collected in 2000 with a grid size of about 6 m. The floating-point elevation values have been retained, which can be especially significant for applications in low topography areas of eastern NC. The elevation data were projected and resampled to 5-m using the default bilinear resampling method to efficiently match UAVSAR data, and then used to derive topography slope and aspect. These three terrain variables were then used as complementary input predictors for the inundation classification model in addition to the primary predictors derived from UAVSAR data, because terrain variables, as key auxiliary predictors, play important roles in determining the distributions of vegetation and water (Wang et al., 2016).

We also acquired several auxiliary datasets that were used in the post-classification processing, including urban impervious surfaces and inundation binary raster layers. Among them, the urban impervious surfaces binary raster layer was extracted from the National Land Cover Database (NLCD; Yang et al., 2018) and used as a control layer to eliminate false positives caused by those urban pixels that were misclassified as inundated forest. Meanwhile, we acquired concurrent multisource inundation maps derived from Landsat-7/8, Sentinel-2, and Sentinel-1 satellite data (mostly acquired on September 18, 2018, see detailed description in Table S5 in Supporting Information S1 of the satellite images used). Specifically, we applied Otsu's method on the spectral water index calculated based on cloud-free optical images (i.e., Landsat-7/8 and Sentinel-2) following previous studies (Yao et al., 2015, 2019). The Sentinel one inundation binary raster data were downloaded from the global flood archive (http://floodobservatory.colorado.edu/Events/4676/GISData/Other/UCONN/) produced by the Dartmouth Flood Observatory at the University of Colorado generated by Shen, Anagnostou, et al. (2019). We applied the Median summary on the multisource inundation scenes together to create a binary inundation raster, which we used as a control layer for excluding false positives classified as open water.

#### 3.1.4. USGS Gage Height Data and River Network Data

In general, the extent of inundation delineated from satellite-based analysis is correlated with corresponding flood hydrographs (Bhatt et al., 2016). To further examine the inundation dynamics, we also collected stream gage height data from the USGS National Water Information System. For each study flight line, there are 2–4 continuously operating streamflow gages managed by the USGS (Figure 1 and Table S7 in Supporting Information S1). We compared the dynamics of inundation extent delineated from UAVSAR with the corresponding same-day observed gage height information.

We used the Hydrological data and maps based on SHuttle Elevation Derivatives at multiple Scales (HydroSHEDS) dataset as a rivers network baseline (Lehner et al., 2008). The river order refers to the backbone discharge order which is calculated based on the long-term average discharge in cubic meters per second using logarithmic progression (Grill et al., 2019).

### 3.2. UAVSAR Processing

We constructed a flood detection algorithm framework (Figure 2) building on previous work by Atwood et al. (2012), including extraction of T3 coherency matrix elements, "Refined Lee Filter" speckle filtering, polarization orientation angle correction, polarimetric decomposition, radiometric terrain correction, radiometric normalization, and supervised classification. The basic processing flow and the auxiliary data sets used are illustrated in Figure 2. The workflow includes three major components. The processing steps in the pink box

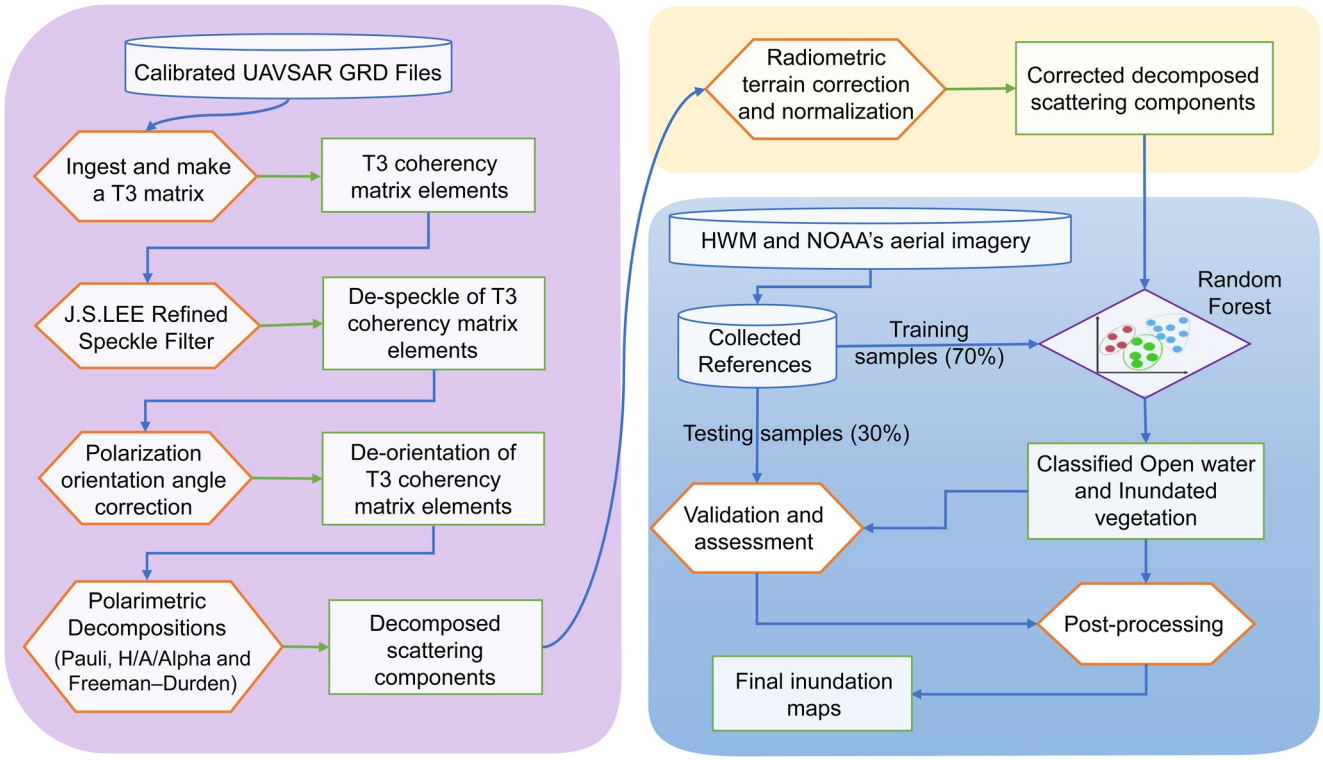


**Figure 2.** The proposed framework for flood inundation mapping from UAVSAR imagery (GRD refers to ground range projected UAVSAR data; T3 refers to coherency matrix derived from quad-polarized SAR data; Pauli, H/A/Alpha, and Freeman-Durden refer to three decomposition methods used here; HWM refers to high-water marks collected by the USGS and NCDEM; the steps in the pink box were carried out via the PolSARpro v6.2 software package; the steps in both yellow and blue boxes were implemented on the GEE platform; the steps in the light blue box make up the supervised classification module.).

were carried out using the European Space Agency (ESA) PolSARpro v6.2 software package (Pottier et al., 2009) through custom python batch scripts. The steps in the light yellow and light blue boxes were implemented in the Google Earth Engine (GEE) platform using the python (v3.7.3) API (v0.1.200) because it provides online cloud computing tools and a flexible interactive development environment, facilitating easy sharing and reproducibility (Gorelick et al., 2017). These steps include radiometric terrain correction, radiometric normalization, and supervised classification modules.

### 3.2.1. Polarimetric De-Speckling and De-Orientation

Speckles appearing in SAR images are caused by the coherent interference of waves reflected from many elementary scatters (Lee et al., 1999). The de-speckling of PolSAR can dramatically boost the performance of image classification (Medasani & Reddy, 2018). Here, we adopted the "Refined Lee Filter" speckle filtering method with a 3 × 3 window based on a tradeoff between spatial resolution and flood detection accuracy discussed in previous studies (Martinis & Rieke, 2015; Ohki et al., 2019). This speckle filtering technique allows us to filter polarimetric data in a fast and simple way while avoiding additional coupling (or cross-talk) between the polarimetric channels (Lee et al., 1999).

In addition to de-speckling, we applied the "Polarization Orientation Compensation" method to perform de-orientation for all UAVSAR images. Without de-orientation, the scattering mechanism may be misjudged in the PolSAR target decomposition step, and may thus lead to overestimation of the volume scattering component induced by topographical slopes (Atwood et al., 2012; Lee & Ainsworth, 2010).

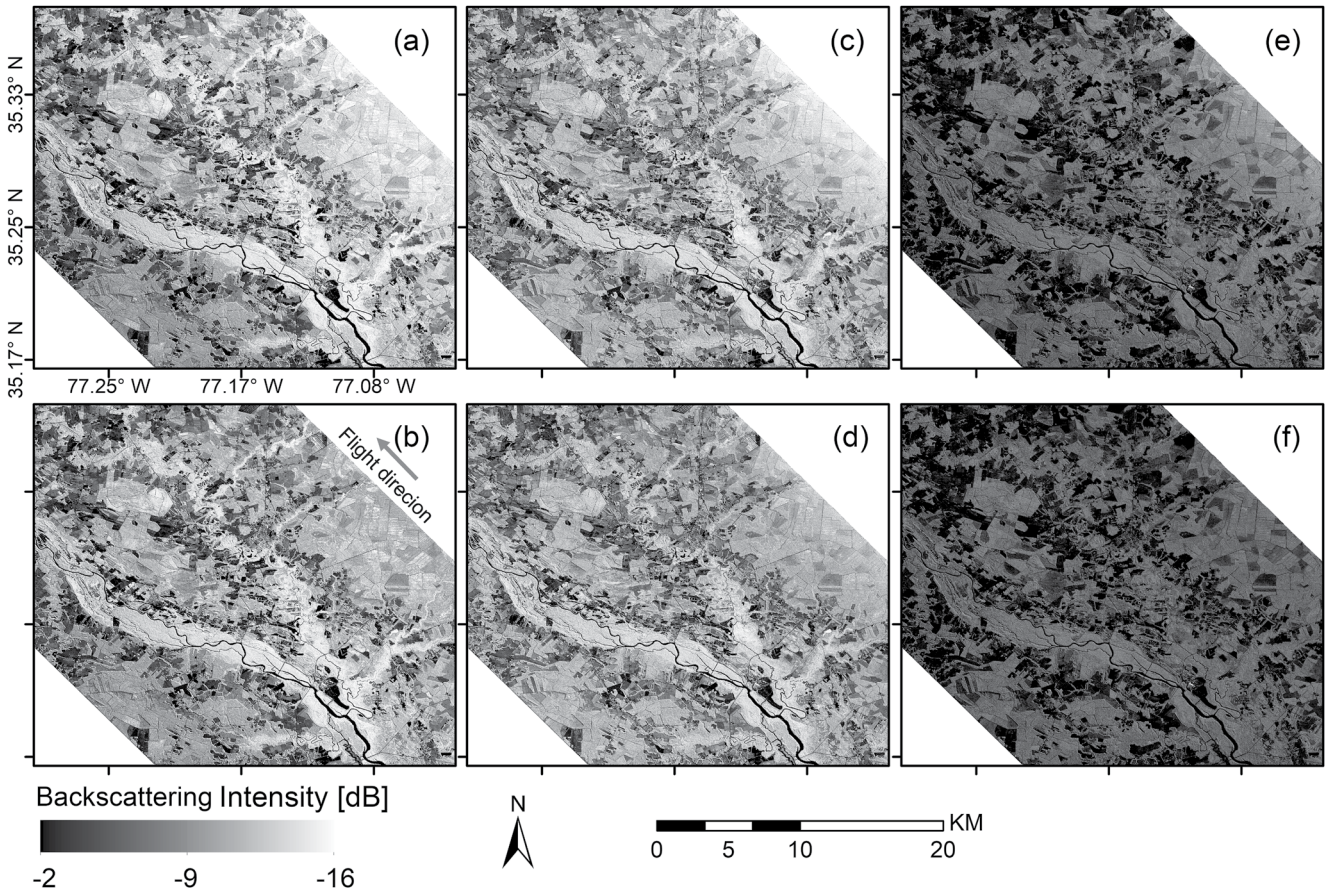


**Figure 3.** UAVSAR polarization intensity GRD images of the Neuse River Flightline on September 18th before and after radiometric normalization at the Neuse River basin near Vanceboro, Craven County, NC. ((a), (c), and (e) refer to the uncorrected HH, VV, and HV image; (b), (d), and (f) refer to the normalized HH, VV, and HV image, the near-to far-range (i.e., from right upper to left bottom). corresponding to incidence angle from about 20° to 70°).

### 3.2.2. Polarimetric Decomposition

Since polarimetric information is sensitive to the geometric structure and physical characteristics of the target, to uncover its physical scattering mechanism, a measured polarimetric matrix can be decomposed into a summation of several dominant scattering mechanisms. Here, to explore the contribution of different physical scattering components derived from PolSAR data in the flood detection model, we adopted three different types of decomposition methods, including Pauli decomposition (PD), Freeman-Durden decomposition (FDD), and H/A/Alpha decomposition (also known as Cloude-Pottier decomposition, CPD) methods (see Methods in Supporting Information for details; Cloude & Pottier, 1997; Freeman & Durden, 1998; Qi et al., 2012). As a result, we derived 10 decomposed polarimetric parameters from each UAVSAR dataset, consisting of three PD parameters, three FDD parameters, and four CPD parameters.

### 3.2.3. Polarization Terrain Correction and Normalization

To correct for topographic effects, we applied the widely used two-stage semi-empirical terrain correction model proposed by Hoekman and Reiche (2015). Since our study area is topographically flat with dense forests but few open areas, the first stage of the model was sufficient to remove most of the topographic effects (Simard et al., 2016).

In addition to topographic effects, the backscatter intensity image shows a clear illumination gradient (e.g., Figures 3a, 3c and 3e) along the span with increasing incidence angle from near to far range due to the side-looking

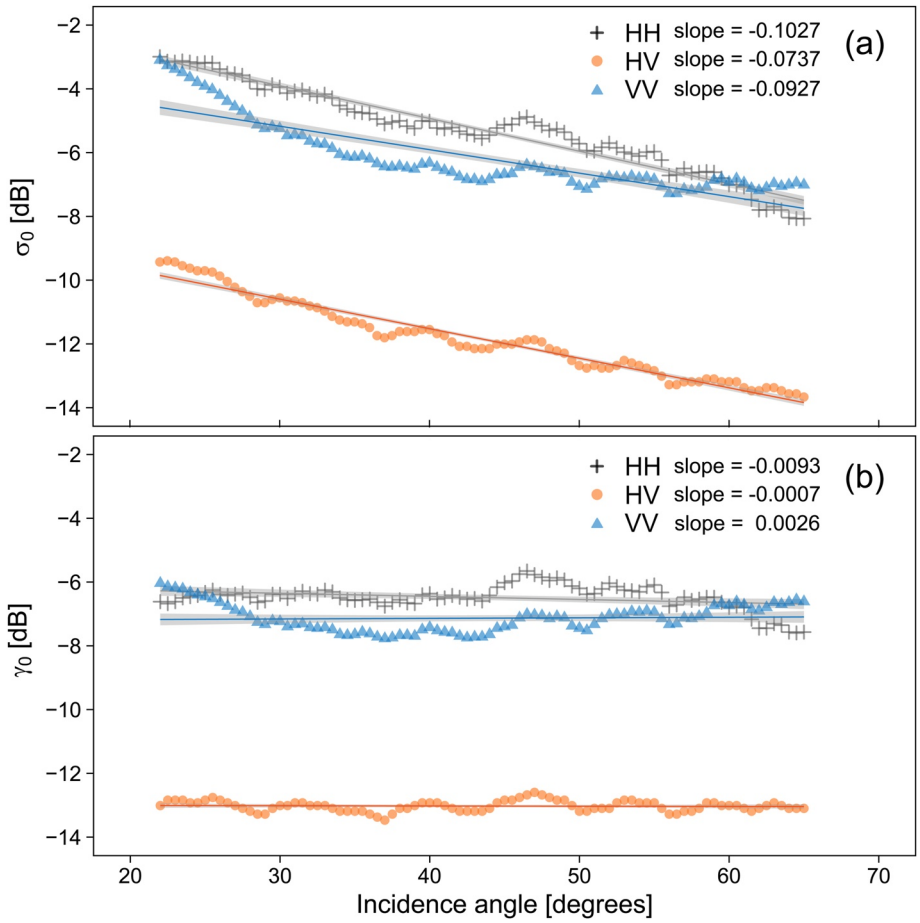


**Figure 4.** The mean of radar backscattering (dB) intensities versus incidence angle along radar range of the Neuse River Flightline on September 18th: Upper panel (a) is the uncorrected data, and the bottom panel (b) shows the normalized results. Straight lines represent linear trends between backscattering intensities and incidence angle using best-fit regression and transparent shades illustrate 95% confidence intervals.

geometry configuration of UAVSAR (Ulaby et al., 1986). In this study, we applied radiometric normalization following Zhang et al. (2017) to correct all UAVSAR polarimetric parameters to the reference incidence angle for any given incidence angle (see Methods in Supporting Information for details). In addition, to make data in different flight lines comparable, the same reference incidence angle (57° equals 180 divided by PI) was adopted in the correction of all UAVSAR flight lines. It should be noted that the normalization procedure here just scales UAVSAR backscattered intensities at different incidence angles to the same intensity of backscattering at the incidence angle of 57°, but it does not correct sensitivity of signal to be the same as observed at 57°. The results that follow are not sensitive to the choice of reference incidence angle in this step.

To evaluate the effectiveness of the correction, we selected four scenes of the flight track covering the Neuse River basin, spanning approximately 130 km from the Cape Lookout National Seashore in the southeast to the city of Greenville in the northwest. Along the cross-range direction, we extracted range profiles of averaged backscattering intensities. Figure 4a presents the extracted range profiles and the corresponding linear regressions of one flight track scene (i.e., September 18th, Flightline ID "neuser_32023_18065_002_180918_L090") in HH, VV, and HV polarizations, which shows the general decrease in backscatter intensity with incidence angle. It is thus important to flatten the observed L-band backscatter along incidence angles to get consistent and comparable values for all incidence angles. In this study, after deriving the corresponding parameters for each scene (e.g., Table S2 in Supporting Information S1), we have successfully flattened the gradient of backscattering intensity along incidence angle (e.g., Figures 3b, 3d, 3f and 4b), which helps to accurately classify flood inundation then. Note that due to the spatial averaging discussed in the preceding section, we ignored the effects of

speckle, geometrical shifts, and other disturbance factors associated with the UAVSAR data. The subtle, nonlinear variations with incidence angle in Figures 4a and 4b are mostly caused by small differences in average land cover types perpendicular to the range direction.

### 3.3. Image Classification Using a Random Forest (RF) Model

For training and validating classification models, we randomly split ground references compiled in Section 3.1.2 into training (70% of each type) and testing (the remaining 30% of each type) datasets. During this step, we discarded testing samples within 2 UAVSAR-pixels (about 10 m) from the closest training samples to avoid validation samples from identical or adjacent pixels, which ensures the generalizability of the subsequently trained models. This resulted in 12,607 training samples and 2,855 testing samples. We applied a Random Forest (RF) classifier on the training dataset to construct flood inundation classification models. In addition to the fact that the GEE platform deploys an easy-to-use RF classifier, the RF classifier has its inherent merit of being quite robust and insensitive to overfitting across many different remote sensing datasets (Breiman, 2001; Gorelick et al., 2017). Moreover, we adopted the RF classifier rather than a deep learning model (e.g., a convolutional neural network) because the computational cost of training a deep learning model is much higher, even though they are becoming increasingly popular and can have superior performance (Denbina et al., 2020; B. Liu et al., 2019).

Here, we established three classification models using three combinations of input variables to explore the contributions of different sets of variables in the flood inundation detection framework. These three models are C1, using linear polarizations only (HH, HV, VV, and HH/VV); C2, using linear polarizations and polarimetric decomposition parameters; and C3, using linear polarizations, polarimetric decomposition and topographic variables. We considered the C1 model as the baseline model because, in most flood detection studies, linear polarizations have commonly been used, since most spaceborne SARs acquire data in single- or dual-polarization mode (Chapman et al., 2015; Hess et al., 2003). With the polarimetric decomposed variables added, the C2 model leverages the scattering mechanisms of inundated targets to generate more accurate flood inundation maps than what has been studied in-depth in previous studies (Clement et al., 2018; Ohki & Shimada, 2018).

To quantify accuracy of each model, we validated the classification models against the testing dataset by calculating producer's accuracy (complement of the Omission Error), user's accuracy (complement of the Commission Error), overall classification accuracy, and Kappa statistics. The original categories of the ground reference samples were reclassified into open surface water (WATR), inundation beneath forest (IBFC), grassland (GRAS), and forest (FORS) to simplify the accuracy analysis between categories that are most critical for understanding flood characteristics (Table S3 in Supporting Information S1).

To assess the importance of input variables in the model, we applied the Boruta algorithm with the 'Boruta' R package, which provides unbiased evaluation via an iteration process (Kursa & Rudnicki, 2010). The experimental results (Figure S2c in Supporting Information S1) indicated that all input variables used in this study are detected as strongly relevant to the flood inundation classification, while the role of most polarimetric parameters from both CPD and FDD were superior to linear polarizations in the classification model.

Based on previous studies (Wang et al., 2015, 2017), we tuned the number of trees (NumTrees), the number of variables per split (NumSplit), and the minimum terminal node (Node) for the RF classification model, identifying the point at which errors stabilized. NumTrees, NumSplit, and Node were set as 800, 8, and 1 to optimize overall accuracy and efficiency (Figures S2a and S2b in Supporting Information S1). The well-trained RF model was subsequently used to produce flood inundation maps of daily repeat-pass UAVSAR scenes on different flight tracks between September 18th and 23rd.

### 3.4. Classification Postprocessing

Despite attempts to obtain the best possible results when performing image classification, the initial classification results, although good, are far from perfect in terms of speckle noise and some other minor errors. To get rid of these effects, postprocessing is an important step to rule out false positives. Especially because the primary goal of this study is to produce a high-accuracy daily time-series of flooding inundation maps to reveal the impacts of Hurricane Florence induced flooding. However, it is worth noting that for most rapid disaster response mapping, post-processing procedures are non-essential option.

In this study, we performed postprocessing procedures on open water and inundated vegetation separately, and then combined them together as the final inundation extent. Specifically, for the open water layer, some non-water pixels may also have lower L-band SAR backscatter values (e.g., man-made flat surfaces and bare soil fields), and therefore be confused with water pixels. We applied a non-inundation exclusion layer based on the synthesized inundation raster data described in Section 3.1.3 to limit commission errors. For the inundated vegetation layer, walls of buildings in urbanized areas cause similar double bounce effects as inundated vegetation. To remedy this, we exclude developed areas from the inundated vegetation layer based on the raster layer of urban impervious surfaces described in Section 3.1.3. In addition, linear backscatter enhancements (i.e., double bounce effects) is also shown in UAVSAR data depending on their geometry (e.g., forest edges oriented parallel to the flight track), resulting in some non-inundated pixels being misclassified as flooded forest (Chapman et al., 2015). To fill small holes in the flooded vegetation binary layer (Figures S3a and S3b in Supporting Information S1) and filter out linear false positives and other isolated flood objects which tend to appear as noise (Figures S3c and S3d in Supporting Information S1), we applied morphological operations (Soille & Pesaresi, 2002) on the flooded vegetation binary layer. First, we applied a closing filter (i.e., a dilation operation followed by an erosion operation) with a 2-pixel radius (i.e., ~10 m) kernel and then a majority filter with a 1-pixel radius kernel to smooth the boundaries of detected flood patches, and finally an opening filter (i.e., the inverse of a closing filter) with a 2-pixel radius. After producing the inundated layer by combining the open surface water and flooded forest layers together, we applied a second set of opening/closing filters to fill holes in the continuous flooded region and further exclude speckle noise but with the kernel size of 4-pixel radius (i.e., ~20 m) to keep a minimum mapping unit of 40 by 40 m as a constraint. We also evaluated the quality of the postprocessing flood inundation extent products (i.e., inundated, or non-inundated binary classes) based on the testing datasets (reclassified as binary classes, see Table S6 in Supporting Information S1).

## 4. Results

### 4.1. Flood Inundation Classification Accuracy

The base model (i.e., model C1 in Table 1) with only linear polarizations achieved a low overall accuracy (OA-75.0%) and Kappa statistic (64.3%). The incorporation of polarimetric decomposition parameters to the base model substantially enhanced the classification of all the class types with overall accuracy and Kappa statistic increased by 14.2% and 20.2%, respectively (i.e., the model C2 in Table 1). Especially for IBFC and FORS classes, the omission errors declined from 27.1% to 7.0% and from 36.8% to 13.4%, respectively. Compared to the base model, the proportion of FORS references misclassified as IBFC was substantially reduced (from 25.7% to 8.5%), indicating the importance of polarimetric decomposition parameters, especially due to the enhanced double-bounce effect. Furthermore, the base model with the addition of polarimetric decomposition and terrain variables (i.e., C3 in Table 1) yielded the highest overall accuracy (94.0%) and Kappa statistic (91.4%). In particular, for WATR and IBFC, the C3 model reduced omission errors for these two classes from 28.8% to 9.6% and from 27.1% to 2.8%, respectively, relative to the base model. However, the main source of the errors observed in the C3 model from the confusion matrices can be attributed to the misclassification between WATR and GRAS (i.e., especially dry grassland, detailed in Table S4 in Supporting Information S1).

### 4.2. Space-Time Patterns in Flood Dynamics

The individual inundation extents derived from UAVSAR images using the above-mentioned method provided direct evidence of river flooding as well as inundation dynamics that occurred in the days following Hurricane Florence. Our results (i.e., Figures 5, 6, 7, 8, S4, and S5) clearly indicated an identifiable change in inundation extents derived from repeat-pass UAVSAR during 5 days' observation (see Figure S6 in Supporting Information S1 for the detailed locations of Figures 5–8, S4, and S5 in Supporting Information S1). To examine inundation dynamics, we analyzed the dynamics of inundation extent delineated from the airborne UAVSAR images with the same-day observed gage height. Specifically, we plotted the time-series inundation extent as points in the "inundation extent versus gage height" plot, calculated from our custom polygons within the adjacent watershed above each gage station.

During September 18–23, in the Swift Creek catchment, a tributary of the Neuse River (Figure 1), inundation extent peaked on September 18th and then decreased over time (Figures 5a–5d), corresponding to the declining

**Table 1**
*Confusion Matrices and Accuracies for the Three Flood Inundation Classification Models (i.e., C1, Linear Polarizations; C2, Linear Polarizations With Added Polarimetric Parameters; and C3: The Same Variables as C2 but With Added Terrain Variables)*

| | WATR | IBFC | GRAS | FORS | *UA (%)* |
|---|---|---|---|---|---|
| **C1: Only polarization variables (HH, VV, HV, and HH/VV)** | | | | | |
| WATR | 551 | 3 | 171 | 3 | 75.69% |
| IBFC | 10 | 290 | 23 | 100 | 68.56% |
| GRAS | 183 | 41 | 1055 | 40 | 79.98% |
| FORS | 19 | 64 | 56 | 246 | 63.90% |
| ***Sum*** | 763 | 398 | 1305 | 389 | |
| ***PA (%)*** | 72.21% | 72.86% | 80.84% | 63.24% | |
| Average PA=72.3%, Average UA=72.0%, OA=75.0%, Kappa=64.3% | | | | | |
| **C2: Addition of decomposition variables** | | | | | |
| WATR | 638 | 5 | 88 | 0 | 87.28% |
| IBFC | 16 | 370 | 0 | 33 | 88.31% |
| GRAS | 102 | 2 | 1201 | 19 | 90.71% |
| FORS | 7 | 21 | 16 | 337 | 88.45% |
| ***Sum*** | 763 | 398 | 1305 | 389 | |
| ***PA (%)*** | 83.62% | 92.96% | 92.03% | 86.63% | |
| Average PA=88.8%, Average UA=88.7%, OA=89.2%, Kappa=84.5% | | | | | |
| **C3: Addition of decomposition and terrain variables** | | | | | |
| WATR | 690 | 1 | 49 | 0 | 93.24% |
| IBFC | 20 | 387 | 5 | 17 | 90.21% |
| GRAS | 51 | 3 | 1250 | 15 | 94.77% |
| FORS | 2 | 7 | 1 | 357 | 97.28% |
| ***Sum*** | 763 | 398 | 1305 | 389 | |
| ***PA (%)*** | 90.43% | 97.24% | 95.79% | 91.77% | |
| Average PA=93.8%, Average UA=93.9%, OA=94.0%, Kappa=91.4% | | | | | |

*Note.* WATR, open surface water, open herbaceous vegetation on flooded water, and sparse tree trunks on flooded water; IBFC, inundation beneath forest canopy; GRAS, wet grassland, dry grassland, fallow cropland, and herbaceous-dominated classes; FORS, upland forest and dry tree-dominated mosaic landscape. The columns are the references, and the rows are the predicted classifications. UA, user's accuracy; PA, producer's accuracy, overall accuracy, and kappa coefficient.

stage at the *Streets Ferry* gage station (USGS 0209205053, Figure 5f). The reduction in inundation extent was about 52.6 km$^2$ (43.9%). We observed that the inundation extent decreased fastest between September 18th and 20th (Figures 5a and 5b), and then it stabilized until the 23rd (Figures 5c and 5d). In the change map shown in Figure 5e, areas near the main channel with the river discharge order of 4 (i.e., 100–1,000 m$^3$/s) did not change significantly (shown in gray), while the flood extent near the tributaries with the discharge order of 5 (i.e., 10–100 m$^3$/s) declined substantially (shown in pink). There was almost no inundation expansion (shown in green) during the study period. We also found that flood inundation changes in the Lumbee (Figure S4 in Supporting Information S1) and Waccamaw (Figure S5 in Supporting Information S1) River basins exhibited similar patterns of spatial variability.

During these five observation dates, the Northeast Cape Fear River Basin witnessed remarkable inundation changes along main and tributary river floodplains (Figures 6a–6e). For the whole observation flight track of the Northeast Cape Fear River Basin, the inundation extent declined by 33.8% (211.4 km$^2$) during the five observation dates compared with the observed inundated extents on the first date (Figures 6a and 6e). The extent of changes in inundation varies at different locations along the river channel (Figure 6f). Specifically, in the drainage area above these two USGS gage stations, the inundation extent shrank by approximately 69.6 km$^2$ (−40.7%) and 150.0 km$^2$ (−45.1%), respectively. We noticed that on the east side of the image downstream of the Chinquapin

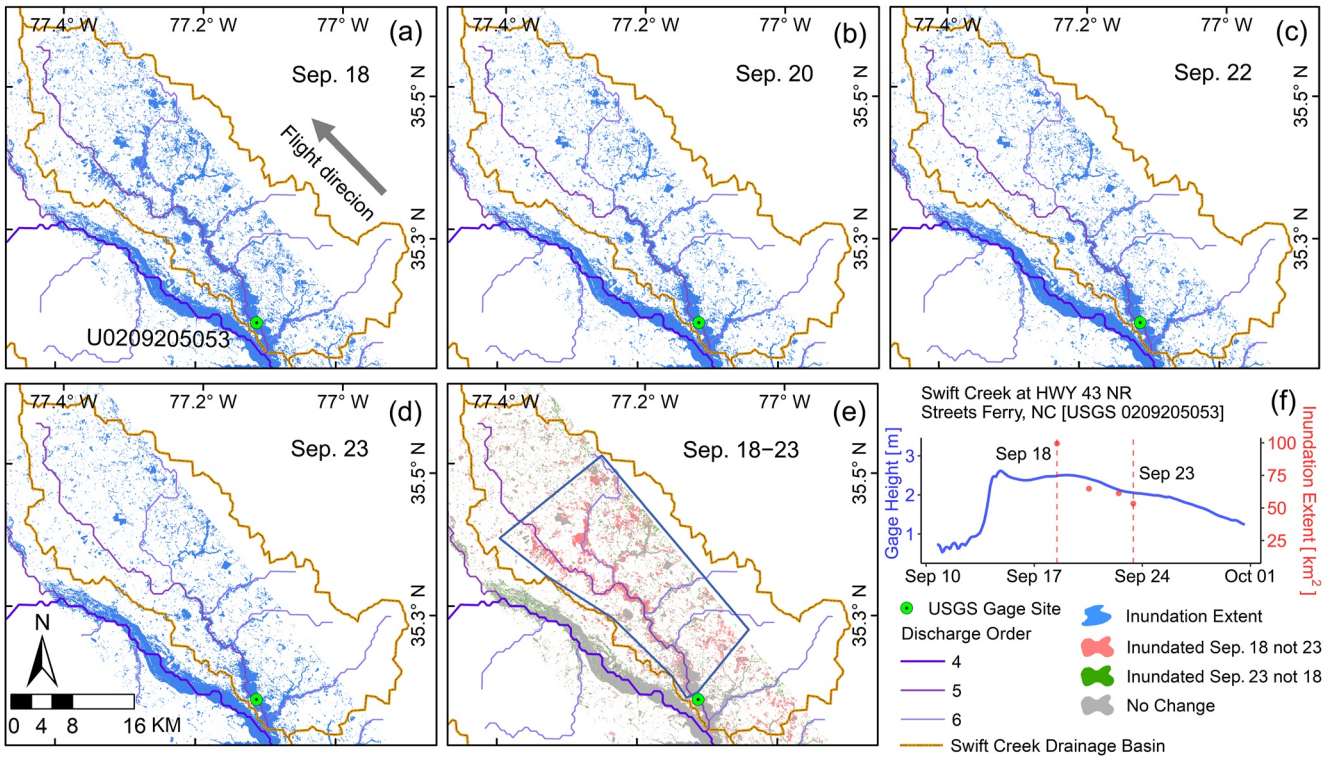


**Figure 5.** Inundation extent maps for the Swift Creek watershed, a tributary of the Neuse River, upstream of Streets Ferry gage station (USGS 0209205053). (a) September 18, 2018; (b) September 20, 2018; (c) September 22, 2018; (d) September 23, 2018; (e) difference between September 18 and 23, 2018, no changes are shown in gray, and the areas flooded only on September 18 in pink; areas flooded only on September 23 in green; (f) inundation extent versus gage height at the Streets Ferry, and the red dots series correspond to UAVSAR-derived inundation extents shown from (a) to (d), calculated over the blue polygon shown in (e). The red dashed lines are the time corresponding to the two UAVSAR observation times in (e).

gage station (USGS 02108000), on September 18th when the water surface elevation was just 1 day past the flow peak (Figure 6g), a usually disconnected channel appeared to be connected, resulting in a temporarily altered network topology (Figure 6a). As the inundation extent declined from September 18th to September 22nd, this channel appeared disconnected again on September 22nd (Figure 6d, marked with a red arrow). Below the Chinquapin gage station, we also found that the flood inundation area was likely at its maximum on September 18th and then decreased over time (Figures 6a–6f), as evidenced by the gage heights at the Burgaw station (Figure 6g).

Figures 7a–7e shows inundation dynamics around the Lower Cape Fear River Basin near the Tar Heel gage station (USGS 02105500) as well as a small watershed above the Big Swamp gage station (USGS 02134480) on September 18th, 19th, 20th, 22nd, and 23rd. Dense time series observations during the flood events captured different peak times in these neighboring watersheds. Specifically, the inundation extent peaks along the Lower Cape Fear River above the Tar Heel gage on September 19th (Figures 7a–7c and 7h, expanded 7.5% (1.5 $km^2$) from September 18th), while the inundation extent above the Big Swamp gage station has already passed its peak on September 18th (Figures 7a, 7b, and 7h). The time series of flood gage heights match the asynchronous dynamics in the inundation extent measurements between the two watersheds (Figure 7h).

In addition to declining inundation extent along most river floodplains, flood inundation extents along the Lower Cape Fear River Basin near the Kelly gage station (USGS 02105769) expanded considerably several days after rainfall (i.e., September 19th, 20th, and 22nd, 2018, Figures 8a–8d). The inundation difference map between September 18th and September 22nd shown in Figure 8e indicates that the inundated area expanded more than 9.5 $km^2$ (16.1%, calculated over the blue polygon within Lower Cape Fear River Basin) within 4 days near the main river channel above the Kelly gage station. This observed change in inundation extent is consistent with gage heights at the Kelly gage station (Figure 8f).

Because of the long and narrow shape and flat slope of the Cape Fear River basin (Figure 1), we observed an interesting phenomenon where flooding in the Lower Cape Fear River near Tar Heel (USGS 02105500) peaked

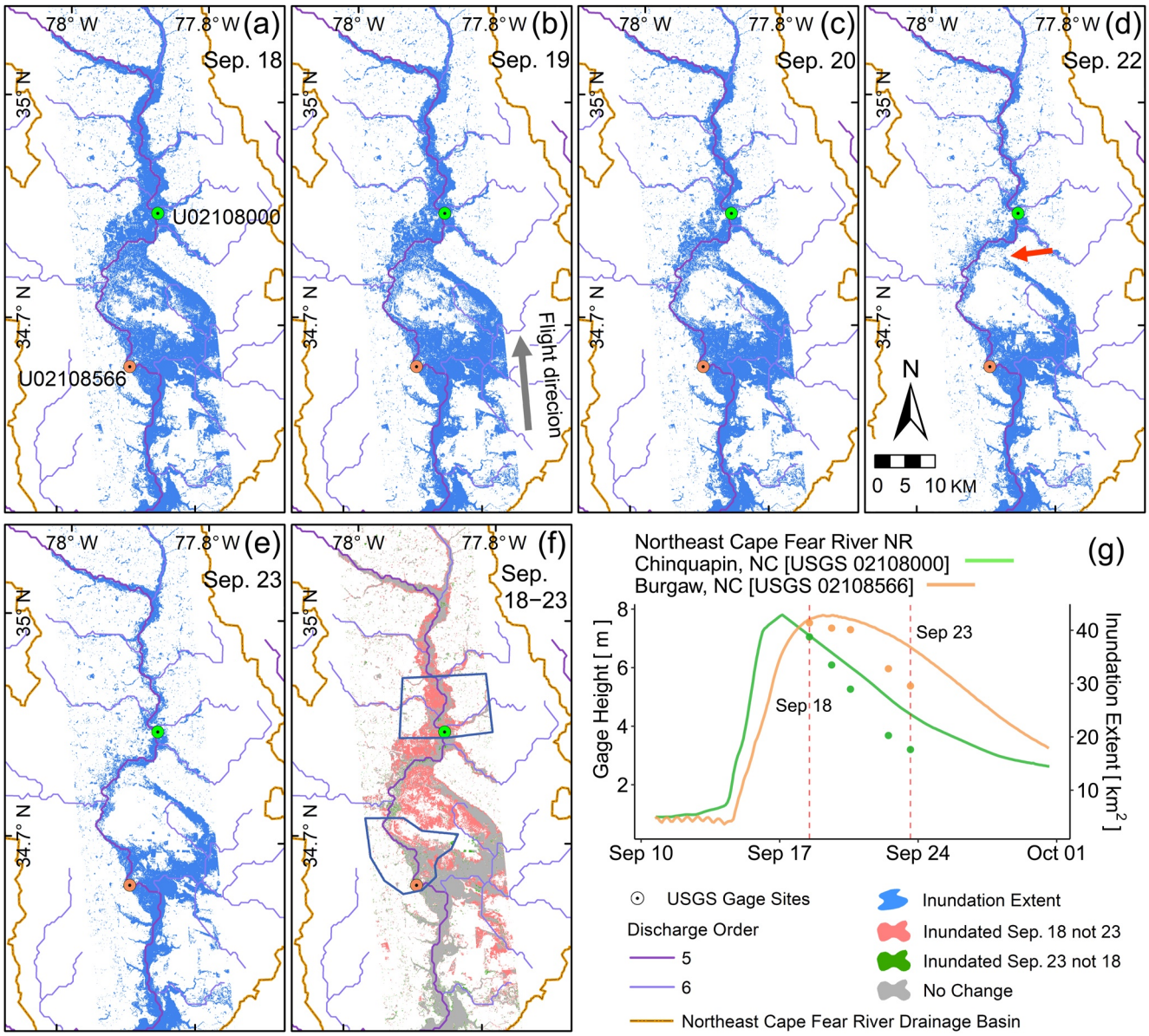


**Figure 6.** Inundation extent maps in the Northeast Cape Fear River Basin. (a) September 18, 2018; (b) September 19, 2018; (c) September 20, 2018; (d) September 22, 2018; (e) September 23, 2018; (f) difference between September 18 and 23, 2018, no changes are shown in gray, and the Areas flooded only on September 18 in pink; areas flooded only on September 23 in green; (g) Inundation extent versus gage height of the Chinquapin (USGS 02108000) and Burgaw (USGS 02108566) gage stations, and the two colored dots series refer to the corresponding time-series UAVSAR observations from (a) to (e), calculated over two blue polygons shown in (f). The red dashed lines are the time corresponding to the two UAVSAR observation times in (f).

on September 19th (Figures 7a and 7h), several days after Florence made landfall, and near Kelly station (USGS 02105769), further downstream, on September 22nd (Figures 8c and 8f). While this pattern is evident from the gage data alone, the remotely sensed imagery provides a comprehensive, near-daily picture of how inundation extent changes spatially in relation to the translation of the flood wave downstream.

Overall, in the aftermath of Hurricane Florence, rapid spatial changes in the flood extents of several major rivers in North Carolina, indicated that the floods receded fast in small tributaries of the Neuse, Cape Fear, Lumbee (Figure S4 in Supporting Information S1), and Waccamaw (Figure S5 in Supporting Information S1) Rivers and near the upper reaches of the Northeast Cape Fear River. Meanwhile, along the flat terrain close to the lower reaches of the Cape Fear River, the flood wave traveled downstream for 4 days after the cessation of rainfall (i.e., September 18th–22nd, 2018).

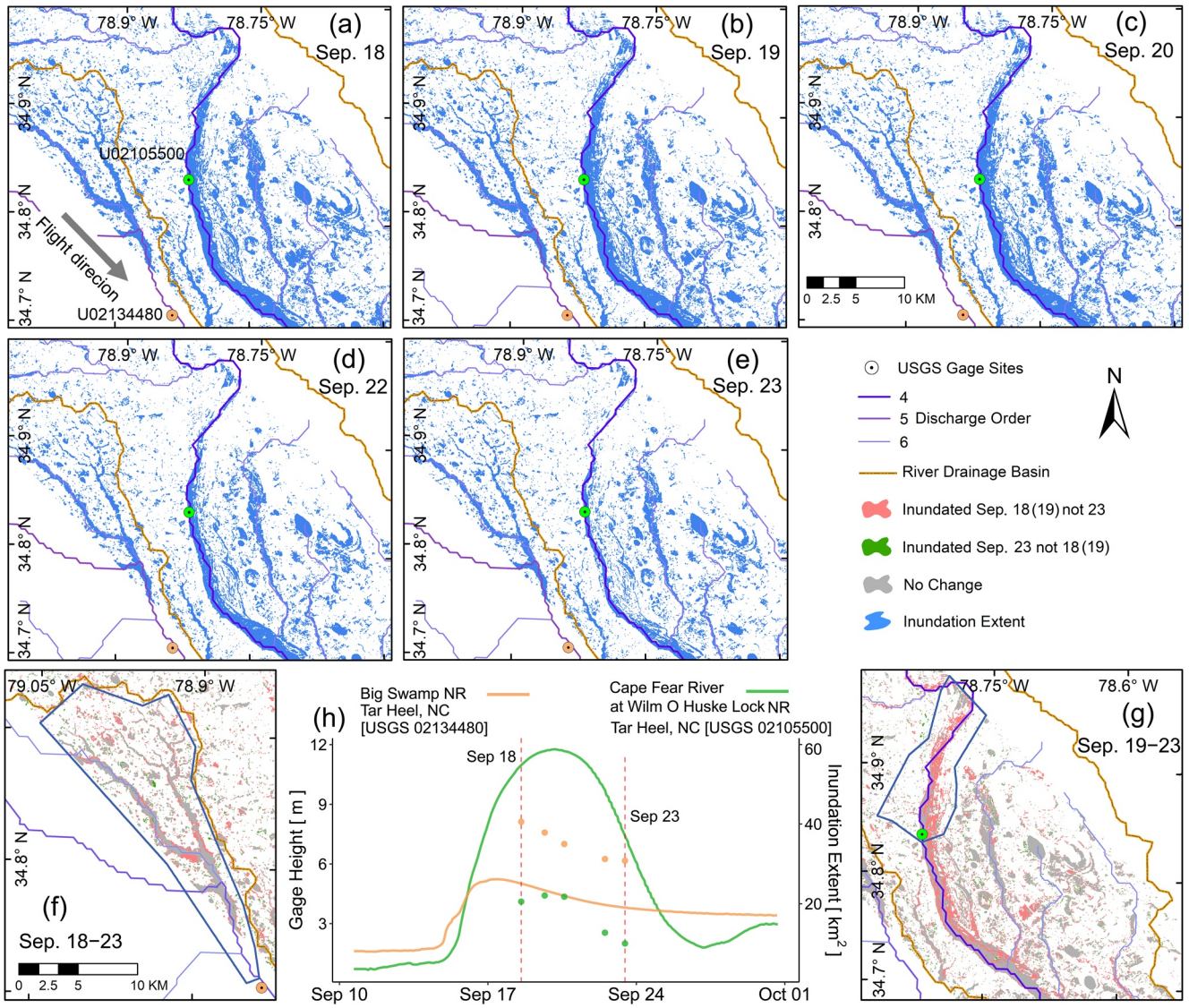


**Figure 7.** Inundation extent maps of the Lower Cape Fear River Basin near the Tar Heel gage station. (a) September 18, 2018; (b) September 19, 2018; (c) September 20, 2018; (d) September 22, 2018; (e) September 23, 2018; (f) difference between September 18 and 23, 2018 along the Big Swamp River; (g) difference between September 19 and 23, 2018 along the Lower Cape Fear River; (h) inundation extents versus gage heights, the center gage site (USGS 02105500) named Cape Fear River near Tar Heel, NC station (called the "Tar Heel station" herein) and the other gage site nearby (USGS 02134480) named Big Swamp near Tar Heel, NC station (called the "Big Swamp station" herein), and the two colored dots series refer to the corresponding UAVSAR observations near the two gage sites from (a) to (e), calculated over the blue polygon shown in (f) and (g). The red dashed lines are the time corresponding to the two UAVSAR observation times in (f).

## 5. Discussion

Accurate and near-real-time monitoring of flood inundation extent is important for disaster response and immediate recovery in flood-prone lowland areas. In addition, understanding the extent of inundation and flood dynamics from past events, particularly in areas that are difficult to monitor, is critical for flood management and mitigation of future flood events. To the best of our knowledge, this is the first study to systematically examine temporal variations in hurricane-induced riverine floods using UAVSAR. Moreover, there has only been few studies using UAVSAR data to estimate inundation extent after a hurricane event (Denbina et al., 2020; Gebremichael et al., 2020); however, it was based on a single day of data collection after Hurricane Harvey (2017). Thus, for the first time, we demonstrate UAVSAR's capacity to map temporal variations in flood inundation extents using daily time series of flood imagery. Based on the analysis of flooding dynamics and ground gage height data, we found that the delineated flood inundation extents in this study clearly captured the rapidly changing inundation

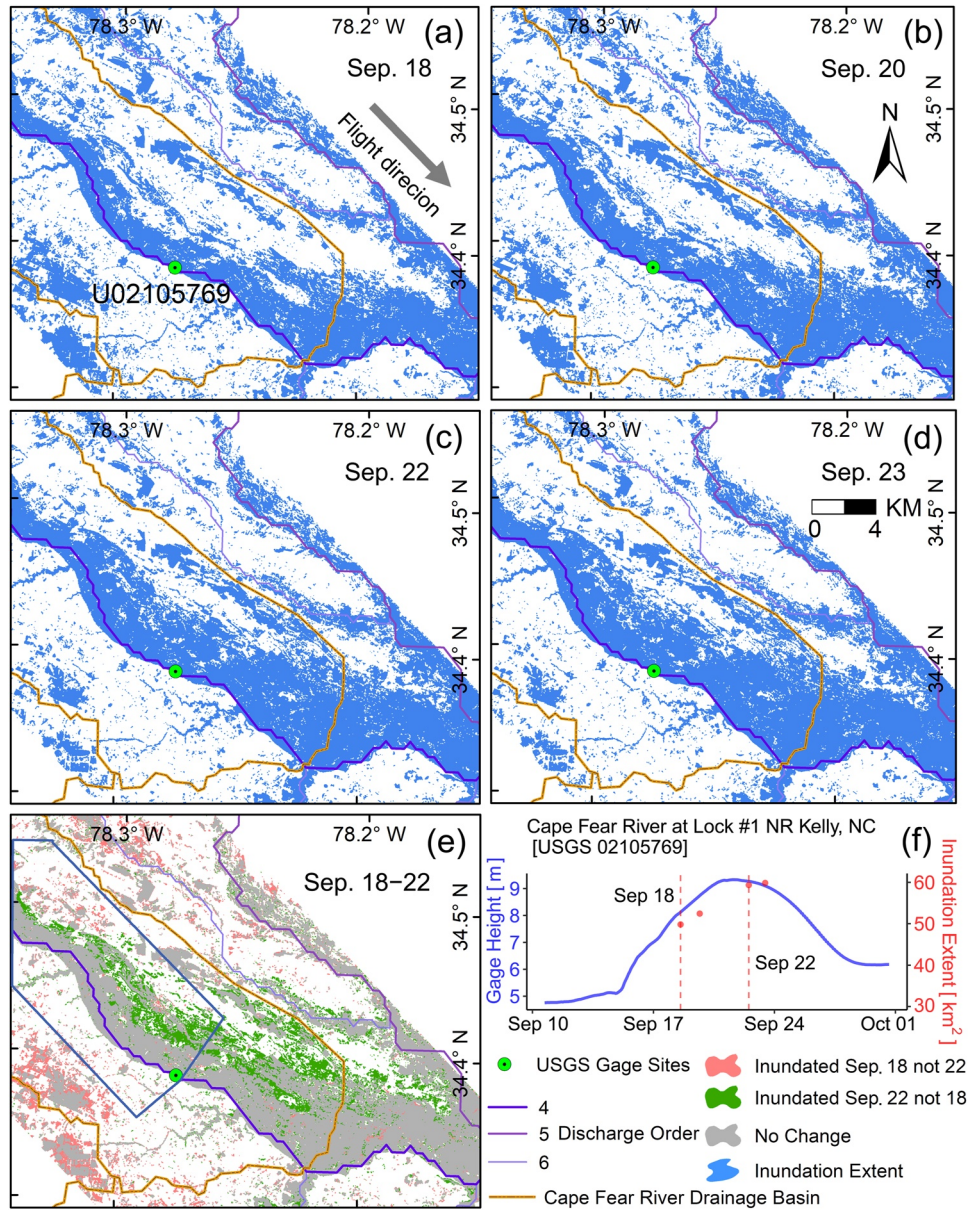


**Figure 8.** Inundation extent maps in the Lower Cape Fear River Basin near Kelly, which is located in the downstream of Figure 7. (a) September 18, 2018; (b) September 20, 2018; (c) September 22, 2018; (d) September 23, 2018; (e) difference between September 18 and 22, 2018; (f) inundation extents versus gage heights from USGS 02105769, Cape Fear River near Kelly, NC. The red dots correspond to the time-series UAVSAR-derived inundation extents from September 18 to 23, 2018, calculated over the blue polygon in (e). The red dashed lines refer to the corresponding time of two UAVSAR observation time show in (e).

extents following Hurricane Florence. The primary advances presented here can be divided into two categories: improvements in remote sensing methods and assessment of hydrologic relevance of UAVSAR data.

### 5.1. Advances in Remote Sensing Methods

From a data acquisition perspective, the UAVSAR platform has increased in popularity not only because the high-resolution repeat-pass data it collects allows monitoring of small surface changes (Rosen et al., 2006; Hensley et al., 2008), but also because it offers a cost-effective solution for near real-time operations as processed data is general available within hours or days. With this fast turnaround time, it serves as a complementary

monitoring tool to existing satellite platforms. In particular, flight paths can be requested (https://uavsar.jpl.nasa.gov/science/flight-requests.html), providing far more flexibility than space-based platforms (Lou et al., 2019). For instance, when encountering a major disaster event, FEMA may submit a rapid disaster response request and acquire new UAVSAR data immediately after the event. This study confirms and highlights the unique value of multitemporal fully-polarimetric SAR data acquired from UAVSAR as a rapid response tool for flood hazards. Given the demonstrated accuracy of the flood inundation classification in this research, it becomes increasingly viable to attain accurate and up-to-date flood disaster response based on UAVSAR. As a result, the UAVSAR platform provides a cost-effective alternative to field survey of flood damage over large areas.

In terms of data processing, based on the literature of multi-polarization SAR data (Whelen & Siqueira, 2017; White et al., 2014; Zhang et al., 2017), this study developed a logically clear and semi-automatic processing pipeline framework connects all tools (i.e., from PolSARpro and GEE) through custom python batch scripts, instead of manual point-and-click operations on the relevant software. This provides the possibility to use our built framework to perform flood inundation mapping in near real-time after collecting UAVSAR data in rapid disaster response to future flood events. UAVSAR collects data at incidence angles between about 20° and 70° from the near-range to the far-range, while larger incidence angles result in weaker contrast between flooded and non-flooded areas because of higher noise levels relative to lower backscatter intensity (Gan et al., 2012). It has been documented in previous studies (Manjusree et al., 2012; Schumann & Moller, 2015; Townsend, 2002) that considering scattering behaviors of floods at different incidence angles is critical to precisely detect flood extent. The normalization function adopted in this study effectively corrects the gradual decrease in brightness of the UAVSAR imagery along the range direction (Figures 3 and 4), thus facilitating the subsequent accurate flood inundation classification of each UAVSAR scene. It is important to note that the normalization method used here would not solve the decreasing double bounce sensitivity as the incidence angle increases. Fortunately, the extracted inundation extents indicated that the detected inundation patches were clear and continuous even at the edge of the images (i.e., incidence angle more than 60° or less than 30°; e.g., Figures 5 and 7). However, the sensitivity of double bounce to incidence angle should be further investigated to ensure that inundated patches at the edges are as accurate as those at the incidence angles between 30° and 60°.

In addition to advanced processing methods, consistent with work by Ohki and Shimada (2018), the classification model based on linear polarizations alone in this study has been able to detect inundation/non-inundation but with relatively low accuracy (i.e., 64.3%). Our analysis shows that HH, VV, and HV polarizations have different contributions to the classification model, but have comparable importance scores (Figure S2c in Supporting Information S1). Our results are consistent with the SAR-based flood-related literature that collectively shows the use of HH is superior to VV polarization for flood area mapping (Manavalan, 2018; Ramsey III et al., 2013). Because HH has a high radiometric dynamic range and tends to penetrate further into the subcanopy, while VV polarization appears to be more sensitive to rough water caused by turbulence or wind (Matgen et al., 2007). Schumann et al. (2007) suggested that in the absence of HH polarization data, the cross-polarization of VH (or HV) is the preferred choice over VV polarization for flood inundation mapping. However, this is not in line with our analysis on the importance of predictor variables. This difference may be due to the use of different wavelengths (i.e., we used L-band, while Schumann et al. (2007) used C-band). In addition, unlike the study of Schumann et al. (2007) which only considered open flooded areas, our study also included inundated vegetation. While VH (or HV) polarization is not affected by double bounce effects and therefore cannot be used to detect inundated vegetation. Ahern et al. (2018) noted that the ratio of HH to VV appears to be a very good indicator for the areas dominated with inundated vegetation, especially in areas with high incidence angles that presented a strong Brewster angle effect (Thirion-Lefevre & Guinvarc'h, 2018). In line with this finding, our study also suggested that the ratio of HH to VV plays an important role in the classification model and its importance ranking is superior to any polarization (Figure S2c in Supporting Information S1).

The addition of polarimetric decomposition features significantly enhanced the accuracy of our method for inundation classification (Table 1). Our results are consistent with the reports that scattering components from PolSAR were particularly advantageous for classifying inundated vegetation (Brown et al., 2016; Hong et al., 2015; Whelen & Siqueira, 2017). In particular, the variable importance test using the Boruta algorithm highlighted that the decomposition variables derived from the CPD and FDD approaches play more important roles in the classification than the linear polarizations (Figure S2c in Supporting Information S1). In addition, the CPD-derived entropy and alpha angle features play a more important role than FDD-derived volume scattering

and double-bounce scattering components in the classification. The knowledge gained here will support future airborne or spaceborne PolSAR missions for relevant hydrological applications such as flood extent monitoring and wetland vegetation mapping (Hong et al., 2015; Lou et al., 2019; Sokol et al., 2004).

The inclusion of terrain variables further improved the accuracy (5%) of the inundation classification model (Table 1), likely because topography affects distributions of both vegetation and surface water. This is especially true for elevation, which is the most important variable in the C3 classification model (Figure S2c in Supporting Information S1). In contrast, the slope and aspect parameters are not as important as elevation because of the relatively flat topography of the study area. This result underscores the unique value of costly historical airborne LiDAR data and revolutionizes our ability to map floods at scales and accuracies that would have been hardly possible without LiDAR.

### 5.2. Advances in Flood Monitoring

Our results highlight that daily flood observations are a major improvement over the less frequent orbital data. Specifically, the dense time series of UAVSAR-derived flood inundation maps can provide detailed information even in highly forested and cloud-prone regions such as North Carolina where optical sensors often fail to provide accurate inundation extent measurements. In addition, our results reveal detailed variability in inundation extent in eastern North Carolina floodplains, consistent with water surface elevations recorded at USGS gages (Figures 5–8, S4, and S5). Specifically, our study reveals altered hydrologic flow pathways not apparent through gage data alone. For example, as illustrated by the red arrow in Figure 6, a temporary hydrologic connection may have routed streamflow away from the main river channel (Figure 6a), which fundamentally changed the river network topology and may have changed the geographic and temporal pattern of downstream flood hazard. This result emphasizes the importance of dense time series flood observations from remotely sensed data. In particular, derived inundation maps can play an important role in data assimilation to real-time coupled hydrologic-hydrodynamic model forecasts (Li et al., 2019). The correctly parameterized hydrologic-hydrodynamic model allows the temporarily altered river network topology in Figure 6a to be highly observable based on gage data. Therefore, it serves as an important tool for flood risk assessment and hazard mitigation planning.

In addition, our method works particularly well in highly vegetated areas where few other methods can supply accurate inundation extent measurements but where floods still have implications on the natural environment and economy. For instance, extended periods of standing water after floods may severely affect forest health and increase potential vulnerability to insect pests and pathogens (Ranger et al., 2013). Based on these hydrologically relevant data and both statistical and hydrodynamic models, future studies could attempt to estimate inundation depth and duration, calculate flood recession rate, and assess flood-prone areas (Grimaldi et al., 2016; Horritt et al., 2007; Hosseiny et al., 2020; Schumann et al., 2010). As extreme weather events like Florence may happen with increasing frequency and intensity under future climate conditions (Bender et al., 2010), a deep understanding of event evolution will help planning future flood mitigation measures and event management.

Regarding the generalizability of the model built in this study, we also examined the feasibility of our established framework for the recent flood event induced by Hurricane Ida on September 1, 2021, without adding local reference data. Specifically, we applied our established framework and trained model C2 on one of the collected UAVSAR scenes (Figure S8 in Supporting Information S1). The results show that the detected inundation extent matches with the locations of levees (Figure S8b in Supporting Information S1), confirming the applicability of our trained model C2 to the updated UAVSAR data of other events. This can be attributed to two factors: on the one hand, the adopted RF classifier has the inherent advantages of being robust and insensitive to overfitting (Breiman, 2001); on the other hand, UAVSAR is a well-calibrated radar system acquiring polarimetric SAR data with an absolute radiometric calibration bias better than 1 dB (Fore et al., 2015). Meanwhile, with the rapid evolution of machine learning models and the continuous accumulation of large amounts of historical flood UAVSAR records, it is worthwhile to acknowledge the importance of establishing a geospatial database that consists of paired ground reference and polarimetric SAR data covering a wide range of landscapes. This is because it will help machine learning models, especially deep learning models, to learn the underlying mapping between polarimetric SAR data and paired ground reference (Denbina et al., 2020; B. Liu et al., 2019), thus further facilitating the generalization of machine learning models to produce reliable inundation maps of different regions.

Compared to physics-based approaches, we agree that they have merits, but as with machine learning models they also have pitfalls (Twele et al., 2016). For example, it is rarely possible to account for all relevant physics, so empirical parameterizations are necessary, which are often challenging to determine. This is particularly true when applying the physics-based approach to the quad-pol SAR data, as in this study, because in addition to open flooded areas, there are extensive flooded areas obscured by vegetation, which complicates the observed flood signals (Plank et al., 2017). As a result, physics-based models built with empirical knowledge may struggle to fully leverage the potential of qual-pol SAR data to achieve high performance. While both approaches are improving with time, we chose to use a machine learning approach because it is relatively simple to implement, does not require full quantification of the physics, and also takes advantage of other auxiliary datasets such as LiDAR-derived terrain data. We anticipate that other studies may make advances in physics-based approaches, and it may ultimately allow the two approaches to complement each other to good effect.

### 5.3. Limitations

Despite these interesting advances, this study has some limitations. First, the most robust validation data available to us, high-water marks, are not collected uniformly or consistently across our study area. In particular, flooded forest types were missing from the field survey data. Although the interpretation of NOAA high-resolution aerial photography (Figure S1a in Supporting Information S1) and PolSAR decomposition data (Figure S1b in Supporting Information S1) in this study contributed to the collection of ground references of inundated forest type, it was dependent on experts' experience and availability of high-resolution aerial photography (Montgomery et al., 2019; Ohki et al., 2019). We acknowledge the methodological limitations of collecting ground references by labeling high-resolution aerial/satellite imagery (e.g., from NOAA, Google Earth, and other sources), which makes our approach labor-intensive for operational applications. By collecting image pairs consisting of ground reference and UAVSAR data from multiple case studies across different landscapes, it would be possible to generate a key empirical database to further train a generalized UAVSAR flood detection model. However, due to the low occurrence of floods, cross-event and image samples are needed in the future to test the generalizability of the proposed method. In addition, the future large-scale operability of the proposed method should consider the radar calibration issue (B. Liu et al., 2019). Although UAVSAR is a well calibrated SAR system, image-specific samples and models may be required considering that the substrate conditions may vary, such as different kinds of vegetation, landscape composition and configuration.

Another limitation is related to the sensitivity of the radar signal itself to flooded targets. Here, we acknowledge that the confusion of the backscattered signals between open surface water and smooth bare soil fields (such as dry grassland, fallow croplands or croplands that have recently been harvested) is an issue in this study, causing overestimation of inundation extents. This problem is in line with observations of Chapman et al. (2015) and Ohki et al. (2019) who reported that some non-flooded pixels were easily misclassified as water and occurred mainly in bare soil or low vegetation areas. In addition, based on daily L-band UAVSAR data, we did notice that backscatter intensity values of smooth fallow fields become progressively lower as the soil becomes drier after flood water receded. This may be because the reduction of moisture in the soil decreases the dielectric constant of the land surface and therefore reduces the amount of radar radiation reflected back, especially in dry soils with low dielectric constant and low radar reflectivity, making the backscattered intensity as low as that of open water (Gallant et al., 2014; Sokol et al., 2004). The fusion of open flood inundation data based on multi-source remotely sensed data substantially reduced the uncertainty of open surface water detection in the post-processing step. This is because optical sensors provide abundant spectral characteristics of ground targets (Tong et al., 2018), which helps to distinguish between open water and bare soil. Thus, we strongly recommend fusion of optical and SAR remotely sensed data for open surface water detection.

In addition, the backscattered signal of the smooth artificial impermeable flat surface, such as that found in urban areas characterized by urban sprawl, also makes it difficult to distinguish from open surface water (Shen, Anagnostou, et al., 2019; Shen, Wang, et al., 2019; Gebremichael et al., 2020). While we only used SAR collected during the flood event, it may be possible to correct this issue if pre-event data is also available. For example, W. Liu and Yamazaki (2018) used both pre-and co-event data to improve the accuracy of extracting flood extent.

Evaluation of the final inundation product after post-processing against the validation reference samples showed an overall accuracy reduction of 2.3% relative to the results of the inundation classification. For omission errors, the erosion operation did help to eliminate many linear-shape false positives at forest edges that occurred frequently

in the landscapes of our study area (Figures S3a and S3b in Supporting Information S1). We note that some reference samples were collected in small, flooded ponds (Figure S7a in Supporting Information S1), and these small isolated water bodies have been filtered out because they do not meet the minimum map unit constraint (i.e., 40 by 40 m). In some other cases, the generated reference samples appeared at the edge of the inundated area (Figure S7b in Supporting Information S1). The boundary smoothing procedure may incorrectly change inundated pixels at edges as non-inundated. In addition, manually digitized ground references may ignore difficult samples, that is, those close to the boundary between inundated and non-inundated classes, because human eyes can easily identify the most evident inundated pixels, but often fail to accurately categorize more challenging samples. For commission errors, the dilation operation may cause non-inundated pixels surrounded by inundated pixels to be mapped as inundated, such as the coastal wetland area of Figure S7c in Supporting Information S1 and partially inundated cropland of Figure S7d in Supporting Information S1. It is worth pointing out that post-processing procedures should be optional and can be tuned for specific applications. For instance, in our riverine flooding monitoring application, it offers improvements in cases where the presence of smooth non-water surfaces (e.g., dry fields) are likely to be misclassified as water. However, if the study targets small ponds and water bodies, we recommend adapting post-processing procedures with caution. Therefore, taken together, our results (Table 1) suggest that our proposed method can be a good candidate for future operational use for quad-polarized SAR data without post-processing.

Some minor limitations should also be noted in this study. Building walls in urban areas may cause foreshortening, layover, and double bounce effects (Cheng et al., 2013; Giustarini et al., 2013), so we masked out urban areas in this study because of their complex backscattering mechanisms and the small proportion of the landscape they represent in the images we studied. In addition, forest edges often exhibit clearly linear backscattering enhancements (i.e., double-bounce effects) in the UAVSAR images (when the forest edges are oriented parallel to the flight track; Chapman et al., 2015), thus leading to misclassification as inundated forest (Figure S3c in Supporting Information S1). These effects can be eliminated to some extent with the erosion operation in post-processing steps.

In addition, for the limitations of monitoring spatial patterns of flood inundation, despite the fact that daily observations are a significant improvement over lower-frequency orbital data, daily observations may still miss high-water events if the high-water periods occur between flights. This situation is particularly likely to occur in areas where flood extent changes rapidly.

### 5.4. Perspectives for Future Research

Flood-related parameters, such as flood onset, maximum extent, and recession, are crucial for stakeholders to understand the impacts of extreme events (Sanyal & Lu, 2004). Although there have been significant advances in satellite-based flood monitoring in recent decades, low temporal frequency observations and persistent clouds have limited our ability to capture these parameters. For example, Clement et al. (2018) suggested that despite the 6-day revisit intervals of Sentinel-1, the sparseness of observations makes it difficult to interpret the data as an accurate representation of the flood time series. Management of future flood events will benefit from the joint SAR constellation of Sentinel-1, PALSAR-2, Radarsat-2, TerraSAR-X, and upcoming NISAR (i.e., NASA ISRO Synthetic Aperture Radar) mission satellites, and other commercial small satellites, such as ICEYE-X2 and Capella Space, thus providing denser time series flood observations.

The inundation extent mapping framework proposed in this study demonstrates that daily UAVSAR observations are capable of monitoring detailed spatially distributed flood dynamics. These flood inundation maps can serve as important validation datasets to reproduce riverine flood dynamics with hydraulic models for supporting flood-resilient communities (Grimaldi et al., 2016). For instance, dense time series of flood inundation maps can help address questions about optimal integration of remote sensing data with hydraulic models. Specifically, Bates et al. (2006) mapped river flood inundation at four time instances with airborne high-resolution (1.2 m) C-band SAR data during the major flood event in 2000 on the River Severn (UK). They used derived inundation maps to assess the performance of a two-dimensional flood inundation model, showing structural weaknesses of the model and suggesting possible future improvements. Further exploration by Horritt et al. (2007) reported that the observations acquired during the receding period were more effective at constraining model predictions than the observations acquired at approximately peak flow. Data such as that used herein could allow further tests of this conclusion in a very different environment.

Additionally, our proposed inundation extent mapping framework demonstrates an excellent means to assist the forthcoming NISAR and SWOT (i.e., Surface Water Ocean Topography) missions during the calibration and validation (Cal/Val) experimental campaign phases. One common objective of these two missions is to measure inundation characteristics (such as inundation extent and water-surface elevation) of inland water bodies or wetland environments with fine spatial resolution and high temporal frequency (Biancamaria et al., 2016; Chapman et al., 2019). Precise and robust measurements of inundation extent derived from UAVSAR, concurrent with SWOT and NISAR overpasses, can complement expensive and time-limiting physical field-based surveys to validate SWOT- and NISAR-derived hydrological characteristics. Especially for SWOT during the 1-day revisit Cal/Val phase, it would be interesting to validate rapidly changing phenomena (e.g., flood events) by comparing with the results of concurrent daily UAVSAR data.

Our results suggested that based on polarimetric decomposition information, quad-pol UAVSAR data enabled the reconstruction of the complete scattering mechanisms rather than backscattering intensity information alone acquired by single- or dual-pol SAR sensors. While spaceborne L-band quad-pol SAR data is not freely accessible to the public yet, NISAR will generate quad-pol L-band SAR images over some targets, holding promise for mapping inundated vegetation with relatively high accuracy. In addition, the important role of polarimetric decomposition information highlights our initial reference categories selection efforts (Tables S3 and S4 in Supporting Information S1), which will help to further explore physical scattering mechanisms of different landscapes. In particular, the applicability of reference categories representing different scenarios is an important factor to consider when collecting ground references, such as the difference in backscatter enhancement by the different canopy cover of flooded trees. It is worthwhile to synergistically use scattering decomposition data with LiDAR datasets to further address this issue in our future works.

Lastly, similar to the cost-effectiveness of LiDAR technology for topographic mapping, the use of UAVSAR technology may become the preferred practice for inundation mapping if costs continue to decrease. As part of ongoing efforts by NASA's Applied Sciences Disaster Program in the Earth Sciences Division, in collaboration with partner agencies, the UAVSAR airborne platform has been utilized to generate rapid disaster response maps, such as flood inundation extents and fire burn areas (Denbina et al., 2020). In addition, the UAVSAR platform has been widely adopted by many ongoing science programs such as NASA's SnowEx, Delta-X, and ABoVE (i.e., Arctic-Boreal Vulnerability Experiment) campaigns, as well as for numerous scientific applications such as monitoring sea ice, oil spills, soil properties, volcano-induced topographic changes, disturbed forest structures, and wetland dynamics (Lou et al., 2019). These varied data collection missions have led it to become a robust and relatively inexpensive platform for rapid data collection over large areas.

## 6. Conclusion

In this study, we proposed a flood extent detection framework for mapping inundation extent using daily, high-resolution (about 5-m), full-polarized L-band UAVSAR data. This framework leverages many tools typically built for PolSAR processing, but it also includes new processing steps, such as the PolSAR normalization and supervised classification implemented on the cloud-computing infrastructure of GEE. We find that the framework proposed here can provide high-quality assessments of catastrophic floods in near-real-time based on UAVSAR data. Furthermore, the incorporation of linear polarizations with polarimetric decomposition (such as CPD and FDD) and terrain variables yielded the best flood extent detection model with a Kappa statistic of 91.4%, increasing by about 27.1% when compared to the baseline model (i.e., only linear polarization), which has been studied in-depth in previous studies. Our analysis showed that the dynamics of inundation extent delineated from daily UAVSAR data aligned with the same-day observed gage height in the aftermath of Hurricane Florence. Although flood wave patterns are evident from the gage data alone, the flood maps derived from UAVSAR data here provide a comprehensive, near-daily picture of how inundation extents vary spatially, for example, inundation extents change locally relative to the translation of the flood wave downstream along the river channel.

In addition, the flood inundation maps produced here are particularly important for successfully filling in flood information gaps in eastern North Carolina, where dense vegetation may hamper flood inundation monitoring with optical data. For instance, they have great potential for assessing flood damages, supporting disaster relief, and assisting hydrodynamic modeling that supports planning for flood-resilient communities.

Since UAVSAR has become a well-established platform for L-band SAR data collection, the method presented in this study provides a way to timely and accurately generate inundation maps with fine spatial resolution and high temporal frequency. This approach provides accurate, dense time-series flood maps for future disaster response and recovery efforts and assists upcoming NISAR and SWOT missions during the calibration and validation (Cal/Val) experimental campaign phases, such as the ability to measure hydrological characteristics in wetland environments.

## Data Availability Statement

The UAVSAR polarimetric data used for this paper are available courtesy of NASA/JPL-Caltech (https://uavsar.jpl.nasa.gov/). We would like to acknowledge the European Space Agency (ESA) Copernicus Sentinel missions that provide the Sentinel-1 and Sentinel 2 data, and thank the U.S. Geological Survey for the provisioning of the Landsat data as well as National Land Cover Database. We give special thanks to Google Earth Engine which provided free access to these archived Landsat 7/8 and Sentinel 2 data as well as computation resources. The derived flood inundation extent dataset associated with this study is available for download from the figshare repository (current version dataset can be accessed through this link for review purpose: https://doi.org/10.6084/m9.figshare.16910878.v5). The code used for processing, mapping, and the analysis in this study can be found at https://github.com/waynechao128/FlorenceFlood_UAVSAR_Repo. All released datasets and information are available under the Creative Commons Attribution 4.0 International (CC-BY 4.0) license (https://creativecommons.org/licenses/by/4.0).

**Acknowledgments**
This research was carried out as a part of the Dynamics of Extreme Events, People, and Places (DEEPP) project at University of North Carolina-Chapel Hill. Funding from a UNC Creativity Hub Award and the National Science Foundation GCR-2021086 is gratefully acknowledged. The authors declare no conflicts of interest relevant to this study. We thank Dr. Jonathan J. Gourley, Dr. Xiaofeng Li, and other two anonymous reviewers for their constructive comments that improved this manuscript. We gratefully acknowledge those who designed, developed, and operate the UAVSAR. We really appreciate PolSARpro and Google Earth Engine developers for their efforts to create these useful tools.

## References

Ahern, F., Brisco, B., Murnaghan, K., Lancaster, P., & Atwood, D. K. (2018). Insights into polarimetric processing for wetlands from backscatter modeling and multi-incidence Radarsat-2 data. *IEEE Journal of Selected Topics in Applied Earth Observations and Remote Sensing*, *11*, 3040–3050. https://doi.org/10.1109/jstars.2018.2850155

Alfieri, L., Bisselink, B., Dottori, F., Naumann, G., de Roo, A., Salamon, P., et al. (2017). Global projections of river flood risk in a warmer world. *Earth's Future*, *5*, 171–182. https://doi.org/10.1002/2016ef000485

Ali, A., Quadir, D. A., & Huh, O. K. (1989). Study of river flood hydrology in Bangladesh with AVHRR data. *International Journal of Remote Sensing*, *10*, 1873–1891. https://doi.org/10.1080/01431168908904017

Atwood, D. K., Small, D., & Gens, R. (2012). Improving PolSAR land cover classification with radiometric correction of the coherency matrix. *IEEE Journal of Selected Topics in Applied Earth Observations and Remote Sensing*, *5*, 848–856. https://doi.org/10.1109/jstars.2012.2186791

Ban, H.-J., Kwon, Y.-J., Shin, H., Ryu, H.-S., & Hong, S. (2017). Flood monitoring using satellite-based RGB composite imagery and refractive index retrieval in visible and near-infrared bands. *Remote Sensing*, *9*, 313. https://doi.org/10.3390/rs9040313

Bates, P. D., Wilson, M. D., Horritt, M. S., Mason, D. C., Holden, N., & Currie, A. (2006). Reach scale floodplain inundation dynamics observed using airborne synthetic aperture radar imagery: Data analysis and modelling. *Journal of Hydrology*, *328*, 306–318. https://doi.org/10.1016/j.jhydrol.2005.12.028

Bender, M. A., Knutson, T. R., Tuleya, R. E., Sirutis, J. J., Vecchi, G. A., Garner, S. T., & Held, I. M. (2010). Modeled impact of anthropogenic warming on the frequency of intense Atlantic hurricanes. *Science*, *327*, 454–458. https://doi.org/10.1126/science.1180568

Benoudjit, A., & Guida, R. (2019). A novel fully automated mapping of the flood extent on SAR images using a supervised classifier. *Remote Sensing*, *11*, 779. https://doi.org/10.3390/rs11070779

Bhatt, C., Rao, G., Diwakar, P., & Dadhwal, V. (2016). Development of flood inundation extent libraries over a range of potential flood levels: A practical framework for quick flood response. *Geomatics, Natural Hazards and Risk*, *8*, 384–401. https://doi.org/10.1080/19475705.2016.1220025

Biancamaria, S., Lettenmaier, D. P., & Pavelsky, T. M. (2016). The SWOT mission and its capabilities for land hydrology. *Surveys in Geophysics*, *37*, 307–337. https://doi.org/10.1007/s10712-015-9346-y

Bioresita, F., Puissant, A., Stumpf, A., & Malet, J.-P. (2018). A method for automatic and rapid mapping of water surfaces from Sentinel-1 imagery. *Remote Sensing*, *10*, 217. https://doi.org/10.3390/rs10020217

Brakenridge, R., & Anderson, E. (2006). *MODIS-based flood detection, mapping and measurement: The potential for operational hydrological applications* (pp. 1–12). Dordrecht: Springer Netherlands.

Breiman, L. (2001). Random forests. *Machine Learning*, *45*, 5–32. https://doi.org/10.1023/a:1010933404324

Brisco, B., Short, N., Sanden, J. v. d., Landry, R., & Raymond, D. (2009). A semi-automated tool for surface water mapping with RADARSAT-1. *Canadian Journal of Remote Sensing*, *35*, 336–344. https://doi.org/10.5589/m09-025

Brown, I., Mwansasu, S., & Westerberg, L.-O. (2016). L-band polarimetric target decomposition of Mangroves of the Rufiji Delta, Tanzania. *Remote Sensing*, *8*, 140. https://doi.org/10.3390/rs8020140

Caballero, I., Ruiz, J., & Navarro, G. (2019). Sentinel-2 satellites provide near-real time evaluation of catastrophic floods in the west mediterranean. *Water*, *11*, 2499. https://doi.org/10.3390/w11122499

Cao, H., Zhang, H., Wang, C., & Zhang, B. (2019). Operational flood detection using Sentinel-1 SAR data over large areas. *Water*, *11*, 786. https://doi.org/10.3390/w11040786

Chaabani, C., Chini, M., Abdelfattah, R., Hostache, R., & Chokmani, K. (2018). Flood mapping in a complex environment using Bistatic TanDEM-X/TerraSAR-X InSAR coherence. *Remote Sensing*, *10*, 1873. https://doi.org/10.3390/rs10121873

Chapman, B., McDonald, K., Shimada, M., Rosenqvist, A., Schroeder, R., & Hess, L. (2015). Mapping regional inundation with spaceborne L-band SAR. *Remote Sensing*, *7*, 5440–5470. https://doi.org/10.3390/rs70505440

Chapman, B., Siqueira, P., Saatchi, S., Simard, M., & Kellndorfer, J. (2019). Initial results from the 2019 NISAR Ecosystem Cal/Val Exercise in the SE USA. In *IEEE International Geoscience and Remote Sensing Symposium (IGARSS 2019)* (pp. 8641–8644).
Cheng, X., Huang, W., & Gong, J. (2013). A decomposition-free scattering mechanism classification method for PolSAR images with Neumann's model. *Remote Sensing Letters*, *4*, 1176–1184. https://doi.org/10.1080/2150704x.2013.858840
Cian, F., Marconcini, M., & Ceccato, P. (2018). Normalized Difference Flood Index for rapid flood mapping: Taking advantage of EO big data. *Remote Sensing of Environment*, *209*, 712–730. https://doi.org/10.1016/j.rse.2018.03.006
Clement, M. A., Kilsby, C. G., & Moore, P. (2018). Multi-temporal synthetic aperture radar flood mapping using change detection. *Journal of Flood Risk Management*, *11*, 152–168. https://doi.org/10.1111/jfr3.12303
Cloude, S. R., & Pottier, E. (1997). An entropy based classification scheme for land applications of polarimetric SAR. *IEEE Transactions on Geoscience and Remote Sensing*, *35*, 68–78. https://doi.org/10.1109/36.551935
Cooper, R. (2018). *Hurricane Florence recovery recommendations*. North Carolina Emergency Management (NCEM).
Denbina, M., Towfic, Z. J., Thill, M., Bue, B., Kasraee, N., Peacock, A., & Lou, Y. (2020). Flood mapping using UAVSAR and convolutional neural networks. In *IGARSS 2020–2020 IEEE International Geoscience and Remote Sensing Symposium* (pp. 3247–3250). IEEE
Dewan, A. M., Islam, M. M., Kumamoto, T., & Nishigaki, M. (2006). Evaluating flood hazard for land-use planning in greater Dhaka of Bangladesh using remote sensing and GIS techniques. *Water Resources Management*, *21*, 1601–1612. https://doi.org/10.1007/s11269-006-9116-1
Dottori, F., Szewczyk, W., Ciscar, J.-C., Zhao, F., Alfieri, L., Hirabayashi, Y., et al. (2018). Increased human and economic losses from river flooding with anthropogenic warming. *Nature Climate Change*, *8*, 781–786. https://doi.org/10.1038/s41558-018-0257-z
Fore, A. G., Chapman, B. D., Hawkins, B. P., Hensley, S., Jones, C. E., Michel, T. R., & Muellerschoen, R. J. (2015). UAVSAR polarimetric calibration. *IEEE Transactions on Geoscience and Remote Sensing*, *53*, 3481–3491. https://doi.org/10.1109/tgrs.2014.2377637
Freeman, A., & Durden, S. L. (1998). A three-component scattering model for polarimetric SAR data. *IEEE Transactions on Geoscience and Remote Sensing*, *36*, 963–973. https://doi.org/10.1109/36.673687
Gallant, A., Kaya, S., White, L., Brisco, B., Roth, M., Sadinski, W., & Rover, J. (2014). Detecting emergence, growth, and senescence of wetland vegetation with polarimetric synthetic aperture radar (SAR) data. *Water*, *6*, 694–722. https://doi.org/10.3390/w6030694
Gan, T. Y., Zunic, F., Kuo, C. C., & Strobl, T. (2012). Flood mapping of Danube River at Romania using single and multi-date ERS2-SAR images. *International Journal of Applied Earth Observation and Geoinformation*, *18*, 69–81. https://doi.org/10.1016/j.jag.2012.01.012
Gebremichael, E., Molthan, A. L., Bell, J. R., Schultz, L. A., & Hain, C. (2020). Flood hazard and risk assessment of extreme weather events using synthetic aperture radar and auxiliary data: A case study. *Remote Sensing*, *12*, 3588. https://doi.org/10.3390/rs12213588
Giustarini, L., Chini, M., Hostache, R., Pappenberger, F., & Matgen, P. (2015). Flood hazard mapping combining hydrodynamic modeling and multi annual remote sensing data. *Remote Sensing*, *7*, 14200–14226. https://doi.org/10.3390/rs71014200
Giustarini, L., Hostache, R., Matgen, P., Schumann, G. J., Bates, P. D., & Mason, D. C. (2013). A change detection approach to flood mapping in urban areas using TerraSAR-X. *IEEE Transactions on Geoscience and Remote Sensing*, *51*, 2417–2430. https://doi.org/10.1109/tgrs.2012.2210901
Gorelick, N., Hancher, M., Dixon, M., Ilyushchenko, S., Thau, D., & Moore, R. (2017). Google Earth Engine: Planetary-scale geospatial analysis for everyone. *Remote Sensing of Environment*, *202*, 18–27. https://doi.org/10.1016/j.rse.2017.06.031
Grill, G., Lehner, B., Thieme, M., Geenen, B., Tickner, D., Antonelli, F., et al. (2019). Mapping the world's free-flowing rivers. *Nature*, *569*, 215–221. https://doi.org/10.1038/s41586-019-1111-9
Grimaldi, S., Li, Y., Pauwels, V. R., & Walker, J. P. (2016). Remote sensing-derived water extent and level to constrain hydraulic flood forecasting models: Opportunities and challenges. *Surveys in Geophysics*, *37*, 977–1034. https://doi.org/10.1007/s10712-016-9378-y
Hallegatte, S., Green, C., Nicholls, R. J., & Corfee-Morlot, J. (2013). Future flood losses in major coastal cities. *Nature Climate Change*, *3*, 802–806. https://doi.org/10.1038/nclimate1979
Heimhuber, V., Tulbure, M., & Broich, M. (2018). Addressing spatio-temporal resolution constraints in Landsat and MODIS-based mapping of large-scale floodplain inundation dynamics. *Remote Sensing of Environment*, *211*, 307–320. https://doi.org/10.1016/j.rse.2018.04.016
Hensley, S., Wheeler, K., Sadowy, G., Jones, C., Shaffer, S., Zebker, H., et al. (2008). The UAVSAR instrument: Description and first results. In *IEEE Radar Conference* (pp. 1–6).
Hess, L. L., Melack, J. M., Filoso, S., & Yong, W. (1995). Delineation of inundated area and vegetation along the Amazon floodplain with the SIR-C synthetic aperture radar. *IEEE Transactions on Geoscience and Remote Sensing*, *33*, 896–904. https://doi.org/10.1109/36.406675
Hess, L. L., Melack, J. M., Novo, E. M. L. M., Barbosa, C. C. F., & Gastil, M. (2003). Dual-season mapping of wetland inundation and vegetation for the central Amazon basin. *Remote Sensing of Environment*, *87*, 404–428. https://doi.org/10.1016/j.rse.2003.04.001
Hoch, J. M., Eilander, D., Ikeuchi, H., Baart, F., & Winsemius, H. C. (2019). Evaluating the impact of model complexity on flood wave propagation and inundation extent with a hydrologic-hydrodynamic model coupling framework. *Natural Hazards and Earth System Sciences*, *19*, 1723–1735. https://doi.org/10.5194/nhess-19-1723-2019
Hoekman, D. H., & Reiche, J. (2015). Multi-model radiometric slope correction of SAR images of complex terrain using a two-stage semi-empirical approach. *Remote Sensing of Environment*, *156*, 1–10. https://doi.org/10.1016/j.rse.2014.08.037
Hong, S.-H., Kim, H.-O., Wdowinski, S., & Feliciano, E. (2015). Evaluation of polarimetric SAR decomposition for classifying wetland vegetation types. *Remote Sensing*, *7*, 8563–8585. https://doi.org/10.3390/rs70708563
Horritt, M. S., Di Baldassarre, G., Bates, P. D., & Brath, A. (2007). Comparing the performance of a 2-D finite element and a 2-D finite volume model of floodplain inundation using airborne SAR imagery. *Hydrological Processes*, *21*, 2745–2759. https://doi.org/10.1002/hyp.6486
Hosseiny, H., Nazari, F., Smith, V., & Nataraj, C. (2020). A framework for modeling flood depth using a hybrid of hydraulics and machine learning. *Scientific Reports*, *10*, 1–14. https://doi.org/10.1038/s41598-020-65232-5
Huang, W., DeVries, B., Huang, C., Lang, M., Jones, J., Creed, I., & Carroll, M. (2018). Automated extraction of surface water extent from Sentinel-1 data. *Remote Sensing*, *10*, 797. https://doi.org/10.3390/rs10050797
Jung, H. C., Hamski, J., Durand, M., Alsdorf, D., Hossain, F., Lee, H., et al. (2010). Characterization of complex fluvial systems using remote sensing of spatial and temporal water level variations in the Amazon, Congo, and Brahmaputra Rivers. *Earth Surface Processes and Landforms: The Journal of the British Geomorphological Research Group*, *35*, 294–304. https://doi.org/10.1002/esp.1914
Kron, W. (2013). Coasts: The high-risk areas of the world. *Natural Hazards*, *66*, 1363–1382. https://doi.org/10.1007/s11069-012-0215-4
Kursa, M. B., & Rudnicki, W. R. (2010). Feature selection with the Boruta package. *Journal of Statistical Software*, *36*, 1–13. https://doi.org/10.18637/jss.v036.i11
Lee, J., & Ainsworth, T. L. (2010). The effect of orientation angle compensation on coherency matrix and polarimetric target decompositions. *IEEE Transactions on Geoscience and Remote Sensing*, *49*, 53–64
Lee, J.-S., Grunes, M. R., & De Grandi, G. (1999). Polarimetric SAR speckle filtering and its implication for classification. *IEEE Transactions on Geoscience and Remote Sensing*, *37*, 2363–2373. https://doi.org/10.1109/36.789635

Lehner, B., Verdin, K., & Jarvis, A. (2008). New global hydrography derived from spaceborne elevation data. *Eos, Transactions American Geophysical Union*, *89*, 93–94. https://doi.org/10.1029/2008eo100001

Li, W., Lin, K., Zhao, T., Lan, T., Chen, X., Du, H., & Chen, H. (2019). Risk assessment and sensitivity analysis of flash floods in ungauged basins using coupled hydrologic and hydrodynamic models. *Journal of Hydrology*, *572*, 108–120. https://doi.org/10.1016/j.jhydrol.2019.03.002

Liu, B., Li, X., & Zheng, G. (2019). Coastal inundation mapping from bitemporal and dual-polarization SAR imagery based on deep convolutional neural networks. *Journal of Geophysical Research: Oceans*, *124*, 9101–9113. https://doi.org/10.1029/2019jc015577

Liu, W., & Yamazaki, F. (2018). Detection of inundation areas due to the 2015 Kanto and Tohoku torrential rain in Japan based on multi-temporal ALOS-2 imagery. *Natural Hazards and Earth System Sciences*, *18*. https://doi.org/10.5194/nhess-18-1905-2018

Lou, Y., Hensley, S., Chapman, B., Hawkins, B., Jones, C., Lundgren, P., et al. (2019). Recent airborne SAR demonstrations for monitoring and assessment of volcanic lava flow and severe flooding. In *IGARSS 2019—2019 IEEE International Geoscience and remote sensing Symposium* (pp. 9388–9390).

Manavalan, R. (2018). Review of synthetic aperture radar frequency, polarization, and incidence angle data for mapping the inundated regions. *Journal of Applied Remote Sensing*, *12*, 021501.

Manjusree, P., Prasanna Kumar, L., Bhatt, C. M., Rao, G. S., & Bhanumurthy, V. (2012). Optimization of threshold ranges for rapid flood inundation mapping by evaluating backscatter profiles of high incidence angle SAR images. *International Journal of Disaster Risk Science*, *3*, 113–122. https://doi.org/10.1007/s13753-012-0011-5

Martinis, S., & Rieke, C. (2015). Backscatter analysis using multi-temporal and multi-frequency SAR data in the context of flood mapping at river Saale, Germany. *Remote Sensing*, *7*, 7732–7752. https://doi.org/10.3390/rs70607732

Martinis, S., Twele, A., & Voigt, S. (2009). Towards operational near real-time flood detection using a split-based automatic thresholding procedure on high resolution TerraSAR-X data. *Natural Hazards and Earth System Sciences*, *9*, 303–314. https://doi.org/10.5194/nhess-9-303-2009

Matgen, P., Schumann, G., Henry, J. B., Hoffmann, L., & Pfister, L. (2007). Integration of SAR-derived river inundation areas, high-precision topographic data and a river flow model toward near real-time flood management. *International Journal of Applied Earth Observation and Geoinformation*, *9*, 247–263. https://doi.org/10.1016/j.jag.2006.03.003

Medasani, S., & Reddy, G. U. (2018). Speckle filtering and its influence on the decomposition and classification of hybrid polarimetric data of RISAT-1. *Remote Sensing Applications: Society and Environment*, *10*, 1–6. https://doi.org/10.1016/j.rsase.2018.02.002

Montgomery, J., Brisco, B., Chasmer, L., Devito, K., Cobbaert, D., & Hopkinson, C. (2019). SAR and Lidar temporal data fusion approaches to boreal wetland ecosystem monitoring. *Remote Sensing*, *11*, 161. https://doi.org/10.3390/rs11020161

Nateghi, R., Bricker, J. D., Guikema, S. D., & Bessho, A. (2016). Statistical analysis of the effectiveness of seawalls and coastal forests in mitigating tsunami impacts in Iwate and Miyagi prefectures. *PLoS One*, *11*, e0158375. https://doi.org/10.1371/journal.pone.0158375

Newcomb, D., & Terziotti, S. (2013). A seamless aggregation of the tiled 20 ft elevation DEM tiles generated by the North Carolina Floodplain Mapping Project. In *U. S. F. a. W. S. a. U. S. G. Survey*. NC State University Libraries. Retrieved from https://www.lib.ncsu.edu/gis/elevation

Ohki, M., & Shimada, M. (2018). Flood-area detection using Palsar-2 data for heavy rainfall disasters in Japan. In *IGARSS 2018—2018 IEEE International Geoscience and Remote Sensing Symposium* (pp. 8777–8780).

Ohki, M., Tadono, T., Itoh, T., Ishii, K., Yamanokuchi, T., Watanabe, M., & Shimada, M. (2019). Flood area detection using PALSAR-2 amplitude and coherence data: The case of the 2015 heavy rainfall in Japan. *IEEE Journal of Selected Topics in Applied Earth Observations and Remote Sensing*, *12*, 2288–2298. https://doi.org/10.1109/jstars.2019.2911596

Plank, S., Jüssi, M., Martinis, S., & Twele, A. (2017). Mapping of flooded vegetation by means of polarimetric Sentinel-1 and ALOS-2/PALSAR-2 imagery. *International Journal of Remote Sensing*, *38*, 3831–3850. https://doi.org/10.1080/01431161.2017.1306143

Pottier, E., Ferro-Famil, L., Allain, S., Cloude, S., Hajnsek, I., Papathanassiou, K., et al. (2009). Overview of the PolSARpro V4.0 software. the open source toolbox for polarimetric and interferometric polarimetric SAR data processing. In *2009 IEEE International Geoscience and Remote Sensing Symposium* (pp. IV-936–IV-939). https://doi.org/10.1109/IGARSS.2009.5417532

Pradhan, B., Tehrany, M. S., & Jebur, M. N. (2016). A new semiautomated detection mapping of flood extent from TerraSAR-X satellite image using rule-based classification and Taguchi optimization techniques. *IEEE Transactions on Geoscience and Remote Sensing*, *54*, 4331–4342. https://doi.org/10.1109/tgrs.2016.2539957

Prein, A. F., Rasmussen, R. M., Ikeda, K., Liu, C., Clark, M. P., & Holland, G. J. (2017). The future intensification of hourly precipitation extremes. *Nature Climate Change*, *7*, 48–52. https://doi.org/10.1038/nclimate3168

Qi, Z., Yeh, A. G.-O., Li, X., & Lin, Z. (2012). A novel algorithm for land use and land cover classification using RADARSAT-2 polarimetric SAR data. *Remote Sensing of Environment*, *118*, 21–39. https://doi.org/10.1016/j.rse.2011.11.001

Qiang, Y. (2019). Disparities of population exposed to flood hazards in the United States. *Journal of Environmental Management*, *232*, 295–304. https://doi.org/10.1016/j.jenvman.2018.11.039

Ramsey, E., III., Rangoonwala, A., & Bannister, T. (2013). Coastal flood inundation monitoring with satellite C-band and L-band synthetic aperture radar data. *JAWRA Journal of the American Water Resources Association*, *49*, 1239–1260. https://doi.org/10.1111/jawr.12082

Ranger, C. M., Reding, M. E., Schultz, P. B., & Oliver, J. B. (2013). Influence of flood-stress on ambrosia beetle host-selection and implications for their management in a changing climate. *Agricultural and Forest Entomology*, *15*, 56–64. https://doi.org/10.1111/j.1461-9563.2012.00591.x

Razavi, S., Gober, P., Maier, H. R., Brouwer, R., & Wheater, H. (2020). Anthropocene flooding: Challenges for science and society. *Hydrological Processes*, *34*, 1996–2000. https://doi.org/10.1002/hyp.13723

Rosen, P. A., Hensley, S., Wheeler, K., Sadowy, G., Miller, T., Shaffer, S., et al. (2006). Uavsar: A new NASA airborne SAR system for science and technology research. In *2006 IEEE Conference on Radar* (p. 8).

Rubel, F., & Kottek, M. (2010). Observed and projected climate shifts 1901–2100 depicted by world maps of the Köppen-Geiger climate classification. *Meteorologische Zeitschrift*, *19*, 135–141. https://doi.org/10.1127/0941-2948/2010/0430

Rueda, A., Vitousek, S., Camus, P., Tomás, A., Espejo, A., Losada, I. J., et al. (2017). A global classification of coastal flood hazard climates associated with large-scale oceanographic forcing. *Scientific Reports*, *7*, 5038. https://doi.org/10.1038/s41598-017-05090-w

Santoro, M., & Wegmüller, U. (2014). Multi-temporal synthetic aperture radar metrics applied to map open water bodies. *IEEE Journal of Selected Topics in Applied Earth Observations and Remote Sensing*, *7*, 3225–3238. https://doi.org/10.1109/jstars.2013.2289301

Sanyal, J., & Lu, X. X. (2004). Application of remote sensing in flood management with special reference to Monsoon Asia: A review. *Natural Hazards*, *33*, 283–301. https://doi.org/10.1023/b:nhaz.0000037035.65105.95

Sayemuzzaman, M., & Jha, M. K. (2014). Seasonal and annual precipitation time series trend analysis in North Carolina, United States. *Atmospheric Research*, *137*, 183–194. https://doi.org/10.1016/j.atmosres.2013.10.012

Schaffer-Smith, D., Myint, S. W., Muenich, R. L., Tong, D., & DeMeester, J. E. (2020). Repeated hurricanes reveal risks and opportunities for social-ecological resilience to flooding and water quality problems. *Environmental Science & Technology*, *54*(12), 7194-7204.

Schumann, G., Di Baldassarre, G., Alsdorf, D., & Bates, P. D. (2010). Near real-time flood wave approximation on large rivers from space: Application to the River Po, Italy. *Water Resources Research*, *46*. https://doi.org/10.1029/2008wr007672

Schumann, G., Hostache, R., Puech, C., Hoffmann, L., Matgen, P., Pappenberger, F., & Pfister, L. (2007). High-resolution 3-D flood information from radar imagery for flood hazard management. *IEEE Transactions on Geoscience and Remote Sensing*, *45*, 1715–1725. https://doi.org/10.1109/tgrs.2006.888103

Schumann, G. J. P. (2014). Fight floods on a global scale. *Nature*, *507*, 169. https://doi.org/10.1038/507169e

Schumann, G. J. P., & Moller, D. K. (2015). Microwave remote sensing of flood inundation. *Physics and Chemistry of the Earth, Parts A/B/C*, *83–84*, 84–95. https://doi.org/10.1016/j.pce.2015.05.002

Shen, X., Anagnostou, E. N., Allen, G. H., Robert Brakenridge, G., & Kettner, A. J. (2019). Near-real-time non-obstructed flood inundation mapping using synthetic aperture radar. *Remote Sensing of Environment*, *221*, 302–315. https://doi.org/10.1016/j.rse.2018.11.008

Shen, X., Wang, D., Mao, K., Anagnostou, E., & Hong, Y. (2019). Inundation extent mapping by synthetic aperture radar: A review. *Remote Sensing*, *11*, 879. https://doi.org/10.3390/rs11070879

Shin, S., Pokhrel, Y., Yamazaki, D., Huang, X., Torbick, N., Qi, J., et al. (2020). High resolution modeling of river-Floodplain-Reservoir inundation dynamics in the Mekong River basin. *Water Resources Research*, *56*, e2019WR026449. https://doi.org/10.1029/2019wr026449

Simard, M., Riel, B. V., Denbina, M., & Hensley, S. (2016). Radiometric correction of airborne radar images over forested terrain with topography. *IEEE Transactions on Geoscience and Remote Sensing*, *54*, 4488–4500. https://doi.org/10.1109/tgrs.2016.2543142

Smith, L. C. (1997). Satellite remote sensing of river inundation area, stage, and discharge: A review. *Hydrological Processes*, *11*, 1427–1439. https://doi.org/10.1002/(sici)1099-1085(199708)11:10<1427::aid-hyp473>3.0.co;2-s

Soille, P., & Pesaresi, M. (2002). Advances in mathematical morphology applied to geoscience and remote sensing. *IEEE Transactions on Geoscience and Remote Sensing*, *40*, 2042–2055. https://doi.org/10.1109/tgrs.2002.804618

Sokol, J., NcNairn, H., & Pultz, T. (2004). Case studies demonstrating the hydrological applications of C-band multipolarized and polarimetric SAR. *Canadian Journal of Remote Sensing*, *30*, 470–483. https://doi.org/10.5589/m03-073

Song, J. Y., Abbaszadeh, P., & Moradkhani, H. (2018). *Future probability of hurricanes and their uncertainties across the south and east coast of the US from Bayesian perspective* (p. A11K-2389). AGU.

Thirion-Lefevre, L., & Guinvarc'h, R. (2018). The double Brewster angle effect. *Comptes Rendus Physique*, *19*, 43–53. https://doi.org/10.1016/j.crhy.2018.02.003

Tong, X., Luo, X., Liu, S., Xie, H., Chao, W., Liu, S., et al. (2018). An approach for flood monitoring by the combined use of Landsat 8 optical imagery and COSMO-SkyMed radar imagery. *ISPRS Journal of Photogrammetry and Remote Sensing*, *136*, 144–153. https://doi.org/10.1016/j.isprsjprs.2017.11.006

Townsend, P. A. (2002). Relationships between forest structure and the detection of flood inundation in forested wetlands using C-band SAR. *International Journal of Remote Sensing*, *23*, 443–460. https://doi.org/10.1080/01431160010014738

Twele, A., Cao, W., Plank, S., & Martinis, S. (2016). Sentinel-1-based flood mapping: A fully automated processing chain. *International Journal of Remote Sensing*, *37*, 2990–3004. https://doi.org/10.1080/01431161.2016.1192304

Ulaby, F. T., Moore, R. K., & Fung, A. K. (1986). *Microwave remote sensing: Active and passive. Volume 3-From theory to applications*. Norwood, MA: Artech House.

UNISDR, C. (2015). *The human cost of natural disasters: A global perspective*.

Wang, C., Gao, Q., Wang, X., & Yu, M. (2015). Decadal trend in agricultural abandonment and woodland expansion in an Agro-Pastoral Transition Band in Northern China. *PLoS One*, *10*(11), e0142113. https://doi.org/10.1371/journal.pone.0142113

Wang, C., Gao, Q., Wang, X., & Yu, M. (2016). Spatially differentiated trends in urbanization, agricultural land abandonment and reclamation, and woodland recovery in Northern China. *Scientific Reports*, *6*, 37658. https://doi.org/10.1038/srep37658

Wang, C., Yu, M., & Gao, Q. (2017). Continued reforestation and urban expansion in the new century of a tropical island in the Caribbean. *Remote Sensing*, *9*, 731. https://doi.org/10.3390/rs9070731

Whelen, T., & Siqueira, P. (2017). Use of time-series L-band UAVSAR data for the classification of agricultural fields in the San Joaquin Valley. *Remote Sensing of Environment*, *193*, 216–224. https://doi.org/10.1016/j.rse.2017.03.014

White, L., Brisco, B., Pregitzer, M., Tedford, B., & Boychuk, L. (2014). RADARSAT-2 beam mode selection for surface water and flooded vegetation mapping. *Canadian Journal of Remote Sensing*, *40*, 135–151

Yang, L., Jin, S., Danielson, P., Homer, C., Gass, L., Bender, S. M., et al. (2018). A new generation of the United States National Land Cover Database: Requirements, research priorities, design, and implementation strategies. *ISPRS Journal of Photogrammetry and Remote Sensing*, *146*, 108–123. https://doi.org/10.1016/j.isprsjprs.2018.09.006

Yao, F., Wang, C., Dong, D., Luo, J., Shen, Z., & Yang, K. (2015). High-resolution mapping of urban surface water using ZY-3 multi-spectral imagery. *Remote Sensing*, *7*, 12336–12355. https://doi.org/10.3390/rs70912336

Yao, F., Wang, J., Wang, C., & Crétaux, J.-F. (2019). Constructing long-term high-frequency time series of global lake and reservoir areas using Landsat imagery. *Remote Sensing of Environment*, *232*, 111210. https://doi.org/10.1016/j.rse.2019.111210

Zhang, M., Li, Z., Tian, B., Zhou, J., & Tang, P. (2016). The backscattering characteristics of wetland vegetation and water-level changes detection using multi-mode SAR: A case study. *International Journal of Applied Earth Observation and Geoinformation*, *45*, 1–13. https://doi.org/10.1016/j.jag.2015.10.001

Zhang, Z., Ni, W., Sun, G., Huang, W., Ranson, K. J., Cook, B. D., & Guo, Z. (2017). Biomass retrieval from L-band polarimetric UAVSAR backscatter and PRISM stereo imagery. *Remote Sensing of Environment*, *194*, 331–346. https://doi.org/10.1016/j.rse.2017.03.034

## References From the Supporting Information

Lee, J.-S., & Pottier, E. (2009). *Polarimetric radar imaging: From basics to applications*. CRC Press.

Menges, C. H., Van Zyl, J. J., Hill, G. J. E., & Ahmad, W. (2001). A procedure for the correction of the effect of variation in incidence angle on AIRSAR data. *International Journal of Remote Sensing*, *22*, 829–841. https://doi.org/10.1080/01431160051060264

## Erratum

In the originally published version of this article, the National Science Foundation funding source number was omitted from the acknowledgments. The acknowledgments have been updated and this version may be considered the authoritative version of record.